A polymorphic element formulation towards multiscale modelling of composite structures

E.S. Kocaman[a,1,*], B.Y. Chen[b], S.T. Pinho[a]

[a] *Department of Aeronautics, South Kensington Campus, Imperial College London. London SW7 2AZ, United Kingdom*
[b] *Faculty of Aerospace Engineering, Delft University of Technology. Kluyverweg 1, 2629 HS Delft, Netherlands*

Abstract

This paper presents a new polymorphic element modelling approach for multi-scale simulation, with an application to fracture in composite structures. We propose the concept of *polymorphic* elements; these are elements that exist as an evolving superposition of various states, each representing the relevant physics with the required level of fidelity.

During a numerical simulation, polymorphic elements can change their formulation to more effectively represent the structural state or to improve computational efficiency. This change is achieved by transitioning progressively between states and by repartitioning each state on-the-fly as required at any given instant during the analysis. In this way, polymorphic elements offer the possibility to carry out a multiscale simulation without having to define a priori where the local model should be located.

Polymorphic elements can be implemented as simple user-defined elements which can be readily integrated in a Finite Element code. Each individual user-defined polymorphic element contains all the relevant superposed states (and their coupling), as well as the ability to self-refine.

We implemented a polymorphic element with continuum (plain strain) and structural (beam) states for the multiscale simulation of crack propagation. To verify the formulation, we applied it to the multiscale simulation of known mode I, mode II and mixed-mode I and II crack propagation scenarios, obtaining good accuracy and up to 70% reduction in computational time —the reduction in computational time can potentially be even more significant for large engineering structures where the local model is a small portion of the total.

We further applied our polymorphic element formulation to the multiscale simulation of a more complex problem involving interaction between cracks (delamination migration), thereby demonstrating the potential impact of the proposed multiscale modelling approach for realistic engineering problems.

Keywords:
Multiscale modelling, Floating Node Method, Mesh Superposition Technique, Fracture, Composites

1. Introduction

1.1. Background

Numerical simulation has evolved drastically in the last decades: for the design of structures, it offers the possibility to reduce considerably design time and cost [1–7]. A particular challenge in numerical simulation of large structures, particularly in composites structures, is the need to simulate the growth of intricate small-scale failure mechanisms. For composite structures, the difference between the length scales (e.g. delamination and matrix cracking are $\mathcal{O} \sim 0.1\,\text{mm}$, while structures are $\mathcal{O} \sim 10\,\text{m}$) can result in prohibitive models if the entire structure is modelled at one single scale.

To address the challenge of modelling large-scale structures, their mechanical response can be simulated using for instance enhanced shell element formulations [8–19] or multi-scale modelling approaches. In the latter, different parts of the structure are modelled at different length scales, time scales, and eventually using different physics, in order to achieve computational efficiency while performing accurate simulations.

We can classify multiscale methods into two families: iterative [20–29] and concurrent [26–38]. In iterative (sub-modelling) approaches [20, 21], a global and a local model are run separately within an iterative procedure. During this iterative procedure, the results from one model determine boundary conditions for the other, until convergence is achieved [20, 21]. In concurrent approaches, a global and a local model are run concurrently, and share a common boundary or overlap region. To enforce kinematic compatibility between the two models, several techniques have been proposed that typically entail the use of appropriate multi-point constraints (MPC) either at the shared boundary or shared overlap region between the two models.

For structural problems, a sudden transition between two types of discretisation can lead to artificial stress concentrations and, in dynamics problems, to stress-wave reflection [34]. Thus, several researchers [33, 34, 38–43] have proposed to use an overlap region between global and local models with different discretisation and/or physics, connected via suitable MPC equations. Concurrent multiscale methods with an overlap region have been used to link continuum to continuum, as well as continuum to structural models [33, 34], continuum to atomistic models [38–41], and continuum with discrete models [42, 43]. In order to achieve efficient multiscale modelling, adaptive modelling approaches have also been proposed, especially in the context of concurrent methods whereby the location of local and global models can be adaptively updated during a numerical simulation [14, 15, 35, 37, 38].

An important difficulty in multiscale modelling of engineering structures is that, while local models typically require a different type of idealisation (e.g. different element types), their location in the structure

*Corresponding author
Email address: e.kocaman15@imperial.ac.uk (E.S. Kocaman)
[1]Tel: +44 7887816544. Address: Department of Aeronautics, South Kensington Campus, Imperial College London, London SW7 2AZ, UK.

may not be known a priori and may even change during the analysis. For effective use within an engineering design environment, multiscale methods should ideally be able to evolve an on-the-fly coupling between local and global models depending on the requirements dictated by the numerical solution at each moment.

Therefore, for the engineering design of engineering structures, there is a strong need for a new multiscale approach whereby local models (with different types of idealisation) can be introduced progressively at any location (and eventually removed as well) during a numerical analysis, as determined by the analysis itself.

1.2. Objective, novelty and outline

The objective of this paper is to propose an original evolving concurrent multiscale model for fracture of engineering composite structures, linking continuum and structural scales. To the authors' knowledge, the multiscale method proposed in this paper is the first where there is an element-level management of the coupling between scales leading to the location and extent of the continuum and structural scales being able to evolve on-the-fly during the analysis as fracture grows. An important characteristic of this conceptually-different numerical framework (including the element-level management of the multiscale aspect) is that it can be readily implemented in most existing FE solvers via a standard user-element interface.

In order to realise this objective, a new type of finite element – a *polymorphic* element – is here formulated so that is capable of transforming its state during a numerical analysis. To illustrate this, Figure 1 shows a wing modelled with shell elements, and subject to a certain in-service evolving loading. If, during this evolving loading scenario, failure initiation were suspected at a certain location (e.g. via any hot-spotting criterion), the *polymorphic* elements in the region of the model surrounding this location would progressively evolve from a shell state to a continuum state. As the damage in the continuum state grew, then the *polymorphic* elements along the prospective damage path would also revert to their solid state so that they could represent damage growth accurately. In this way, an adaptive multi-scale modelling methodology can be achieved at an element level enabling increased control over the desired computational accuracy and efficiency during a numerical simulation.

In the example above, because only the areas near damage at any moment would be modelled with continuum elements (without having had to assume beforehand where damage would start), the use of *polymorphic* elements would enable a particularly powerful multiscale modelling framework. However, the concept of *polymorphic* elements is not restricted to the simulation of damage growth and to continuum-to-structural coupling: the different states in *polymorphic* elements can in general represent other scales (e.g. nano-scale), different numerical methods (e.g molecular dynamics, lattice methods, etc...), different physics (e.g. electro-magnetic, thermal, etc...), and parametrised components (e.g. stiffeners, joints).

The proposed element concept uses floating node method in order to represent each state. The advantages of using FNM for a (semi-) concurrent approach are:

- By using FNM, we can exploit various advantages inherent to FNM, relatively to other damage modelling methods such as XFEM and PNM, as documented in [44]. Among these, the main advantage is the increased control over element partitioning without re-meshing;
- FNM can treat complex 3D crack propagation problems, as demonstrated for instance in [45] where notched and unnotched composite specimens were modelled with over 100 cracks modelled explicitly; and
- specifically with regard to application examples used in our manuscript, using FNM enables the representation of a beam with a combination of continuum and beam elements through the thickness of the beam (see Figure 26a). This representation would not be trivial for instance with PNM.

Additionally, an advantage of the proposed polymorphic element concept over other (semi-) concurrent approaches is that the former enables superposition of different states at element level, thereby lending itself more readily to a flexible numerical framework where different states and coupling between them can be achieved inside a suitable user-defined element. Overall, the methodology provides a conceptually simpler modelling approach for multi-scale problems.

The *polymorphic* element concept proposed uses the Floating Node Method [44], which is reviewed in Sections 2 and 3, and the Mesh Superposition Technique [34], which is reviewed in Section 4. The formulation of *polymorphic* elements is then detailed in Section 5. The *polymorphic* element was then implemented for several 2D examples. In section 6, Double Cantilever Beam, End Notch Flexure and Mixed Mode Bending configurations are used to validate the implementation in pure Mode I, pure Mode II and Mixed Mode crack growth problems for which there is a closed-form analytical solution. With the purpose of demonstrating applicability to a situation of engineering relevance, a delamination migration test is also shown in section 7; this migration test has been developed recently by NASA Langley Research Centre to evaluate the capability of numerical methods in predicting crack migration [46]. The results are discussed in Section 8 and conclusions are drawn in Section 9.

2. Floating Node Method

As shown in Figure 2, in FNM [14, 44, 45, 47–50], in addition to standard nodes, elements also have floating nodes. These floating nodes are not tied to an initial position, but are instead associated with any geometrical (topological) entities, such as edges, surfaces or volumes.

With standard finite elements, when a discontinuity passes through the element, additional Degrees of Freedom (DoFs) are typically needed to represent the discontinuity. Instead, in FNM, floating nodes are assigned to the positions of the discontinuities to form sub-elements inside the main element. Then, typical

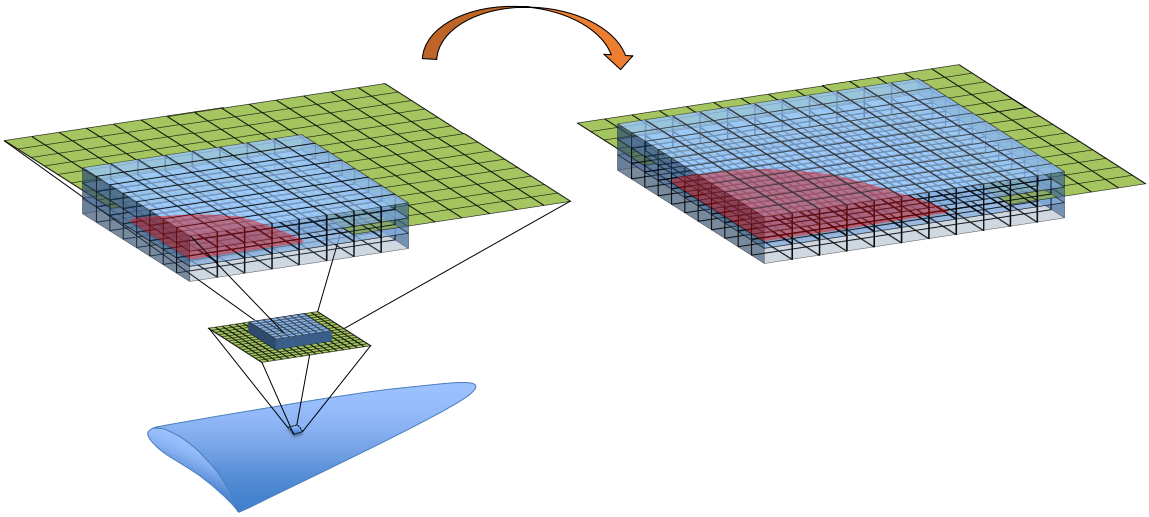

Figure 1: Polymorphic element concept (the representative damage is shown in red)

finite element calculations are performed for all sub-elements each occupying a separate part of the domain (Figure 2).

In FNM, different enrichments of the elements with floating nodes can be considered for different applications [14, 44, 45, 47–50].

In the literature, FNM has been applied for the modelling of matrix crack density saturation and interactions between matrix cracks and delaminations in a cross-ply laminate [44]. In the same work, it was coupled with Virtual Crack Closure Technique (VCCT) and an edge status variable approach to evolve discontinuities inside the material [44]. FNM was also shown to provide more accurate stress intensity factors (SIFs) compared with PNM [44]. In another work [47], delamination migration in cross-ply tape laminates was modelled with FNM.

Recently, Chen et al. [45] implemented a 3D version of FNM, and used it to model tensile failure of composites. The edge status variable approach was used for the automatic propagation of matrix cracks in the mesh. The work demonstrated that 3D FNM is capable of capturing multiple damage modes in the progressive failure of composites such as matrix crack formation, grip-to-grip longitudinal splits, delaminations, fibre breaking and bulging out in the 0° plies. Additionally, FNM was successfully applied to shell elements for delamination modelling [14]. For a detailed description of the FNM, the reader is referred to [44, 45, 47].

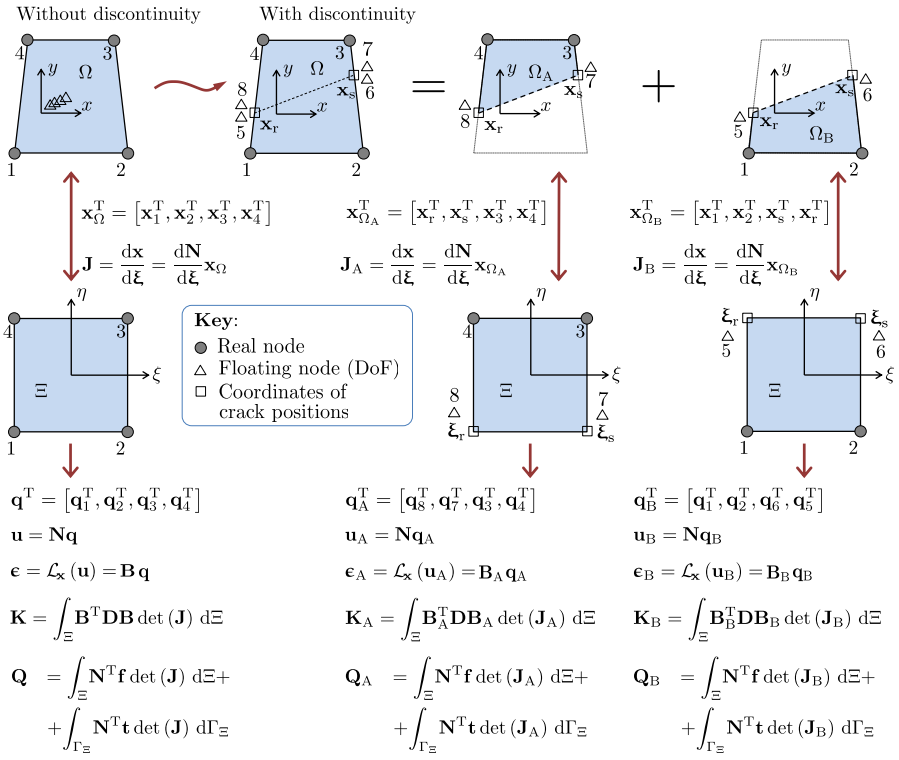

Figure 2: Overview of the Floating node method, after [44]

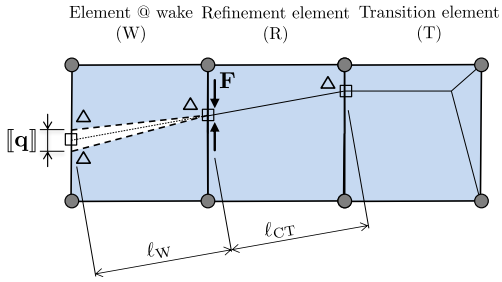

Figure 3: Implementation of VCCT with FNM, from [44]

3. Implementation of progressive damage simulation techniques with FNM

3.1. Introduction

Cohesive zone models and VCCT are both very widely used to represent crack growth numerically. The application of these with FNM is detailed in this section.

3.2. Application of VCCT using FNM

Consider the numerical representation of a crack shown in Figure 3. According to VCCT, the energy release rates for mode I and mode II are given respectively by [51]:

$$G_{\mathrm{I}} = \frac{1}{2A_{\mathrm{W}}} F_{\mathrm{n}} [\![q_{\mathrm{n}}]\!] \left(\frac{A_{\mathrm{W}}}{A_{\mathrm{CT}}} \right)^{1/2}, \tag{1}$$

$$G_{\mathrm{II}} = \frac{1}{2A_{\mathrm{W}}} F_{\mathrm{t}} [\![q_{\mathrm{t}}]\!] \left(\frac{A_{\mathrm{W}}}{A_{\mathrm{CT}}} \right)^{1/2}, \tag{2}$$

where F_{n} and F_{t} are the components of force $\mathbf{F}$ in the normal and tangential directions, and $[\![q_{\mathrm{n}}]\!]$ and $[\![q_{\mathrm{t}}]\!]$ are the components of displacement jump $[\![\mathbf{q}]\!]$ in the normal and tangential directions of the crack, respectively [44]. Also, A_{W} represents the crack surface area in the wake element (for a 2 dimensional problem, $A_{\mathrm{W}} = \ell_{\mathrm{W}} b$, where ℓ_{W} is the length of the discontinuity in the wake element as shown in Figure 3 and b is the thickness of the domain) and A_{CT} is the crack surface area in the refinement element (for a 2 dimensional problem, $A_{\mathrm{CT}} = \ell_{\mathrm{CT}} b$, where ℓ_{CT} is the length of the discontinuity in the refinement element as shown in Figure 3). Using the energy release rates calculated with Equations 1 and 2, a criterion of the form

$$f(G_{\mathrm{I}}, G_{\mathrm{II}}, G_{\mathrm{Ic}}, G_{\mathrm{IIc}}, \eta) = 0, \tag{3}$$

where G_{Ic}, G_{IIc} and η are relevant material properties, can be employed to decide whether the crack should propagate. Then, the elements can be partitioned using FNM and the crack can be propagated accordingly.

3.3. Application of cohesive zone models using FNM

Considering a crack composed of initially coinciding surfaces that are separated by applied tractions, Cohesive Zone Models (CZM) [52] introduce a cohesive zone where the traction is related to the respective separation of the respective initially-coinciding surfaces through a constitutive law.

Cohesive cracks can be readily integrated to a cracked element using FNM as shown in Figure 4. Considering an element that has failed and partitioned into two regions (Ω_A and Ω_B), a cohesive sub-element can easily be integrated to the element along the discontinuity surface $\Gamma_{\Omega_\mathrm{c}}$ (see Figure 4). The stiffness matrix for the overall domain Ω of the element can be written as

$$\mathbf{K}_\mathrm{all} = \int_{\Omega_\mathrm{A}} \mathbf{B}_\mathrm{A}^\mathrm{T} \mathbf{D} \mathbf{B}_\mathrm{A} \, \mathrm{d}\Omega + \int_{\Omega_\mathrm{B}} \mathbf{B}_\mathrm{B}^\mathrm{T} \mathbf{D} \mathbf{B}_\mathrm{B} \, \mathrm{d}\Omega + \int_{\Gamma_{\Omega_\mathrm{c}}} \mathbf{N}_\mathrm{CE}^\mathrm{T} \mathbf{D}_\mathrm{CE} \mathbf{N}_\mathrm{CE} \, \mathrm{d}\Gamma_\mathrm{c}, \tag{4}$$

where $\mathbf{B}_\mathrm{A}$ and $\mathbf{B}_\mathrm{B}$ are strain-displacement matrices for the domains Ω_A and Ω_B. $\mathbf{N}_\mathrm{CE}$ is the shape function matrix for the cohesive element that relates the nodal DoFs along $\Gamma_{\Omega_\mathrm{c}}$ to the separations and $\mathbf{D}_\mathrm{CE}$ refers to the constitutive matrix that relates the cohesive traction to the respective crack jump.

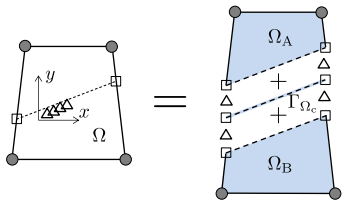

Figure 4: Integration of cohesive elements, from [44]

Therefore, the floating nodes along the surface $\Gamma_{\Omega_\mathrm{c}}$ can directly interpolate the displacement jumps across the cohesive interface. Finally, the stiffness matrix of the cohesive sub-element can be assembled locally to the stiffness matrix of the floating node element, together with those of Ω_A and Ω_B as shown in Equation 4.

4. Mesh superposition technique

Consider a body with two domains A and B which have different physics and/or discretization. With the Mesh Superiposition Technique (MST), a transition (or hand-shake) region is introduced between the two differently-discretized domains (see Figure 5); a part of each domain is included in the transition region and their contribution is superposed using weight functions (that verify partition of unity condition) and the level set method [53].

Considering Figure 5, the stiffness matrix of an element in the transition region can be written as

$$\mathbf{K} = \sum_{i \in \{\mathrm{A},\mathrm{B}\}} \int_{\Omega_i} \mathbf{B}_i^\mathrm{T} \mathbf{D}_i \mathbf{B}_i w_i \, \mathrm{d}\Omega, \tag{5}$$

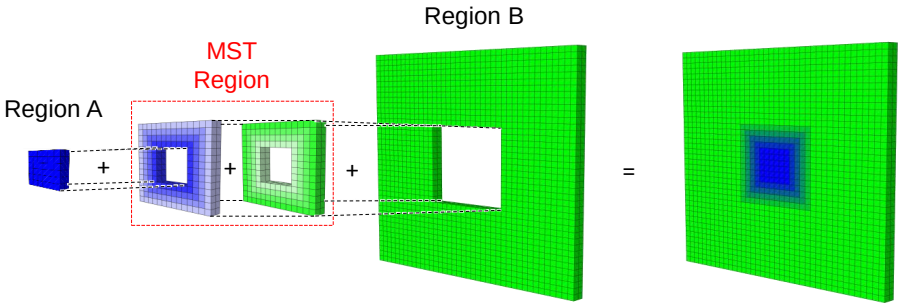

Figure 5: MST schematic, after [34]

with

$$\sum_{i\in\{\mathrm{A,B}\}} w_i = 1, \tag{6}$$

where $\mathbf{B}$ and $\mathbf{D}$ refer to the shape function matrix and constitutive matrix of the individual regions, respectively. $\mathbf{K}$ represents the overall stiffness matrix of the element, and w is a weight function.

The weight functions vary monotonically along the MST region between the two domains, and a level set method [53] is used to compute their value at an individual element. Consider the MST region shown in Figure 6. For point P in region Ω_s, with a coordinate $\mathbf{x}$, the weight functions w_A and w_B can be calculated using the following steps:

(i) the unsigned distances between P and the boundaries Γ_A and Γ_B (see Figure 6) are

$$d_\mathrm{A} = \|\mathbf{x}_\mathrm{A} - \mathbf{x}_\mathrm{P}\|, \tag{7}$$

$$d_\mathrm{B} = \|\mathbf{x}_\mathrm{B} - \mathbf{x}_\mathrm{P}\|, \tag{8}$$

where $\mathbf{x}_\mathrm{A}$ and $\mathbf{x}_\mathrm{B}$ refer to the position vectors of the closest points (A and B) to P on Γ_A and Γ_B;

(ii) the distance d between the closest points A and B, as well as the projected signed distances a and b along the line connecting the closest points respectively (see Figure 6) can be written as

$$d = \|\mathbf{x}_\mathrm{B} - \mathbf{x}_\mathrm{A}\|, \tag{9}$$

$$a = \frac{|(\mathbf{x}_\mathrm{B} - \mathbf{x}_\mathrm{A}) \cdot (\mathbf{x}_\mathrm{A} - \mathbf{x}_\mathrm{P})|}{d}, \tag{10}$$

$$b = \frac{|(\mathbf{x}_\mathrm{B} - \mathbf{x}_\mathrm{A}) \cdot (\mathbf{x}_\mathrm{B} - \mathbf{x}_\mathrm{P})|}{d}, \tag{11}$$

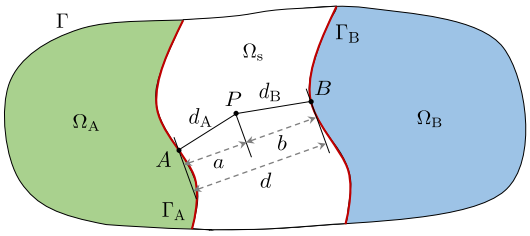

Figure 6: Computation of weight functions (after [34])

(iii) then, the weight functions w_{A} and w_{B} become

$$w_{\mathrm{A}} = \begin{cases} 0 & \Leftarrow \quad a > d \\ b/d & \Leftarrow \quad a, b < d \\ 1 & \Leftarrow \quad b \geq d \end{cases}, \tag{12}$$

$$w_{\mathrm{B}} = \begin{cases} 0 & \Leftarrow \quad b > d \\ a/d & \Leftarrow \quad a, b < d \\ 1 & \Leftarrow \quad a \geq d \end{cases}. \tag{13}$$

This technique was applied in a finite element analysis to simulate the low-velocity impact of a projectile on a composite plate [34]. The results demonstrate that artificial stress disturbances between the domains can be avoided and MST can capture the delamination and crack patterns due to the impact at a lower computational cost than a model with a sudden transition. Further demonstrations for the absence of stress concentrations and stress-wave reflections when using the MST method are provided in reference [54].

Although the concept holds in 3D, in the current implementation, 2D demonstration examples are presented and the weight functions become 1D functions.

5. Development of a *polymorphic* element

5.1. Element description

We propose the concept of a *polymorphic* element which consists of n elements existing in a state of evolving superposition (see Figure 7). Each of the superposed elements represents the same region of the domain, but with different types of idealisation, level of detail, and computational cost. The stiffness matrix $\mathbf{K}$ of a *polymorphic* element is given by

$$\mathbf{K} = \sum_{i=1}^{n} w_i \mathbf{K}_i, \tag{14}$$

where the weight functions w_i change in time t and verify partition of unity

$$\sum_{i=1}^{n} w_i(t) = 1, \tag{15}$$

and $\mathbf{K}_i$ are the stiffness matrices of the superposed elements expanded to the total number of DoFs.

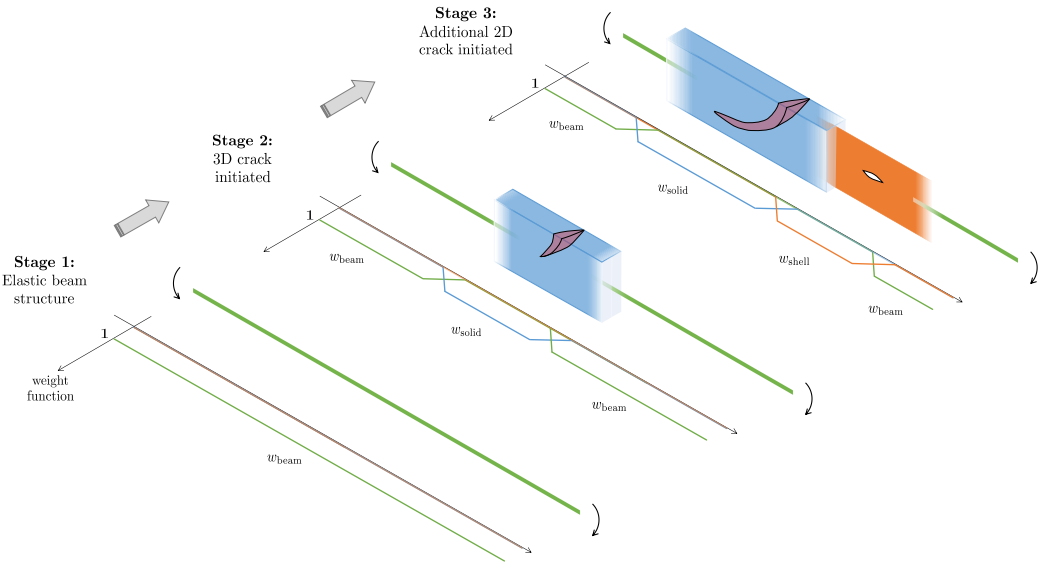

Figure 7: Schematic representation of an FE mesh composed of polymorphic elements. As different types of damage initiate and grow, the state of superposition within each element evolves accordingly

Each of the superposed elements, with stiffness matrix $\mathbf{K}_i$ may represent a given region of the domain using different types of idealization (e.g. continuum vs. structural elements) and different levels of detail (e.g. different mesh p- and h-refinements). Additionally, each superposed element may re-partition itself as needed using FNM (e.g. to represent an evolving geometry during crack growth).

The weight functions w_i are calculated and updated during the analysis using a level-set method so as to represent, at each moment during the analysis, each region of the domain with the required idealization and detail.

Note that, while the example in Figure 7 only requires the weight functions to be 1D functions, in general there is no restriction for w to be 1D. For instance, in Figure 1, w would not be a 1D function. A fully generic 3D function for w is possible with the MST; however, the computational implementation would become more complex which may not be ideal for the initial demonstration of the *polymorphic* concept.

Polymorphic elements are aimed at problems where a higher level of detail is only required in a small part of the domain, but whose location may evolve during the analysis (such as damage growth regions). In this type of problems, by deactivating all unused DoFs at each step, the use of polymorphic elements leads naturally to a computationally-efficient fully-coupled evolving multiscale method.

5.2. A polymorphic *element for solid/beam transition*

To demonstrate the *polymorphic* element concept as explained in Section 5.1, the detailed formulation for a *polymorphic* element consisting of the superposition of solid and beam elements is here presented in detail (see Figure 8).

The element consists of real nodes (filled circles in Figure 8) and floating nodes (empty triangles in Figure 8) that are either shared by adjacent elements (edge nodes) or belong uniquely to the element (internal nodes). The real nodes (full circles in Figure 8) provide the position information of the element

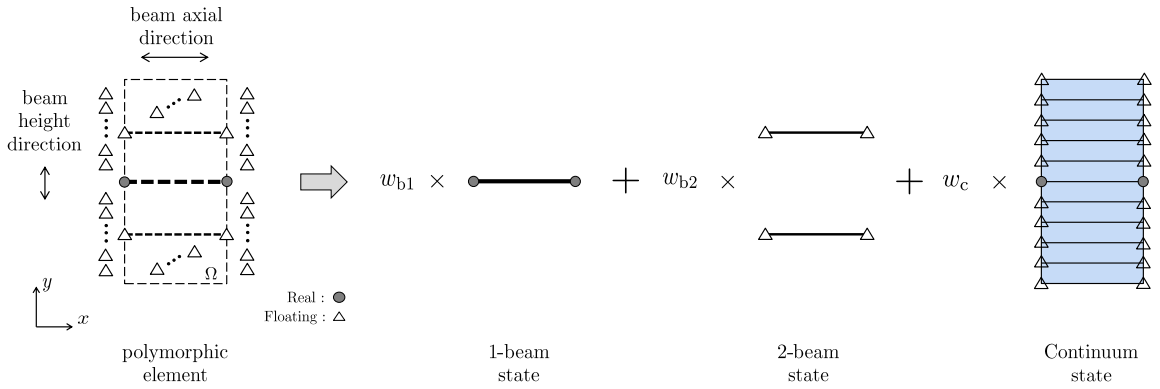

Figure 8: Polymorphic element topology for a beam (with axis along the x direction), consisting of three superposed states: a '1-beam' state, a '2-beam' state and a continuum state

along the neutral axis of the beam structure, whereas the floating nodes are used to build-up the thickness of the structure explicitly when using solid elements. Each of the floating nodes is activated or deactivated depending on the required topology in the respective region during a numerical analysis.

This *polymorphic* element acts as a master element that evolves, i.e. it can transform into different element types, their superposition and sub-partition to model damage. The exact state of the element during the analysis is defined on-the-fly based on the position of the element relatively to a delamination crack tip (see Figure 9) using a level-set method to define the weight functions (Equation 14).

The equilibrium equations for the element can be written by summing the individual contributions of the (expanded) beam and continuum element stiffness matrices ($\mathbf{K}_{b1}$, $\mathbf{K}_{b2}$ and $\mathbf{K}_c$, respectively) multiplied by their corresponding weight functions (w_{b1}, w_{b2} and w_c respectively):

$$w_{b1}\mathbf{K}_{b1} + w_{b2}\mathbf{K}_{b2} + \sum_{j=1}^{n_c} w_c \mathbf{K}_c^j = \mathbf{f}^{ext}, \tag{16}$$

$$w_{b1} + w_{b2} + w_c = 1, \tag{17}$$

where n_c represents the number of solid elements that compose the continuum state of the polymorphic element and $\mathbf{f}^{ext}$ represents the external force vector. In Equation 16, the stiffness matrix $\mathbf{K}_c$ for the

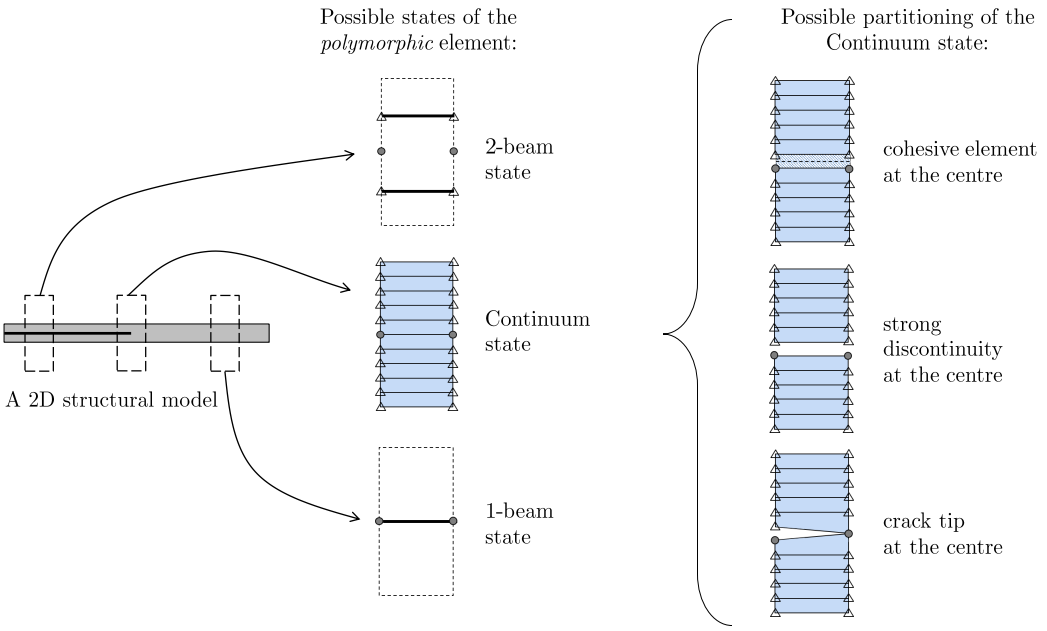

Figure 9: Different states of the *polymorphic* element

continuum state of the *polymorphic* element consists of the sum of the (expanded) stiffness matrices $\mathbf{K}_{\mathrm{c}}^{j}$ of each sub-element j of the continuum state. This partitioning of the continuum state can itself evolve during the analysis as shown in Figure 9.

For the *polymorphic* element shown in Figure 9, at each cross-section of the beam, the multipoint constrains that link the solid state to the '1-beam' state ensure compatibility between the rotation of the beam and the rotation that can be calculated from the horizontal displacements of the continuum elements. Identically, the multipoint constrains that link the solid state to the '2-beam' state ensure compatibility between the rotation of the top/bottom beam and the rotation that can be calculated from the horizontal displacements of the top/bottom half of the continuum elements. Note that the '1-beam' and '2-beam' states are not allowed to coexist via choice of the evolution laws for the weight functions (i.e. $w_{\mathrm{b1}} \neq 0 \implies w_{\mathrm{b2}} = 0$ and vice versa).

The crack tip position is used to define the location of two transition regions, each with a pair of transition lines A and B as in Figure 6. With reference to Figure 9, let transition region 2 be the transition between the '2-beam' state and the continuum state, and let transition region 1 be the transition between the continuum state and the '1-beam' state. Then, in-line with the MST formulation presented in Section 4, the weight

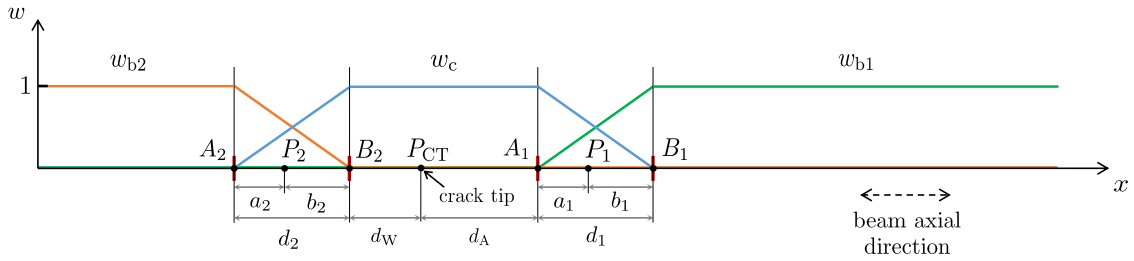

Figure 10: Implementation of the MST in 1D

functions become

$$w_{b1} = \begin{cases} 0 & \Leftarrow \quad b_1 > d_1 \\ a_1/d_1 & \Leftarrow \quad a_1, b_1 < d_1 \\ 1 & \Leftarrow \quad a_1 \geq d_1 \end{cases}, \tag{18}$$

$$w_c = \begin{cases} 0 & \Leftarrow \quad a_1 > d_1 \quad \text{and} \quad b_2 \geq d_2 \\ b_1/d_1 & \Leftarrow \quad a_1, b_1 < d_1 \\ a_2/d_2 & \Leftarrow \quad a_2, b_2 < d_2 \\ 1 & \Leftarrow \quad b_1 \geq d_1 \quad \text{and} \quad a_2 \geq d_2 \end{cases}, \tag{19}$$

$$w_{b2} = \begin{cases} 0 & \Leftarrow \quad a_2 > d_2 \\ b_2/d_2 & \Leftarrow \quad a_2, b_2 < d_2 \\ 1 & \Leftarrow \quad b_2 \geq d_2 \end{cases}, \tag{20}$$

where a_1, d_1, b_1 and a_2, d_2, b_2 are the distances associated to the MST zones between the continuum state and '1-beam' state and '2-beam' state, respectively, as per Figure 10. Considering the crack tip P_{CT} with coordinate x (in Figure 10), the distances a_1, d_1, b_1 and a_2, d_2, b_2 can be calculated using the user-defined distances for the wake (d_W) and ahead (d_A) of the crack tip as well as MST zone lengths (d_1, d_2), using:

$$a_1 = |x_{P_1} - x_{P_{CT}} - d_A|, \tag{21}$$

$$b_1 = |x_{P_1} - x_{P_{CT}} - d_1 - d_A|, \tag{22}$$

$$a_2 = |x_{P_2} - x_{P_{CT}} + d_2 + d_W|, \tag{23}$$

$$b_2 = |x_{P_2} - x_{P_{CT}} + d_W|, \tag{24}$$

where x_{P_1} and x_{P_2} indicate the positions of the points that are in the MST zones 1 and 2, respectively. In order to implement the adaptivity with the proposed method, each of the *polymorphic* elements has access to information that defines the crack tip (P_{CT} in Figure 10) and calculates its weight functions using

Table 1: Elasticity related material properties for IM7-8552 [55]

E_{11} (GPa)	$E_{22} = E_{33}$ (GPa)	$\nu_{12} = \nu_{13}$	ν_{23}	$G_{12} = G_{13}$ (GPa)	G_{23} (GPa)
161	11.38	0.32	0.44	5.17	3.98

Table 2: Fracture and strength related material properties for IM7-8552 [55]

G_{Ic} (kJ/m^2)	G_{IIc} (kJ/m^2)	η	Y_{t} (MPa)	S (MPa)	k (N/mm^3)
0.21	0.77	2.1	60	90	10^6

Equations 18, 19 and 20.

6. Verification

6.1. Introduction

In order to verify the proposed element, several test cases involving crack propagation were used. These tests included Double Cantilever Beam (DCB), End-Notch Flexure (ENF), and Mixed Mode Bending (MMB), see Figure 11. The test cases were simulated using both cohesive zone theory and VCCT to demonstrate the capability of the method to integrate different damage simulation techniques. Mesh convergence and parametric studies were conducted to understand the effect of different system features on the simulation results. The analytical solutions for the test cases were used as a benchmark for verification.

In all of the test cases, the specimen has an initial crack $a_0 = 30\,\mathrm{mm}$ (Figure 11). Following De Carvalho et al. [47], specimens width $w = 25.4\,\mathrm{mm}$ and length $2L = 100.8\,\mathrm{mm}$. The thickness of the specimens $2h$ is $3\,\mathrm{mm}$ with each arm having $1.5\,\mathrm{mm}$ thickness. The material properties are given in Tables 1 and 2.

Figure 12 illustrates the application of the *polymorphic* FNM to simulate the tests. The *polymorphic* elements were formulated such that the region around the crack tip was modelled with continuum elements whereas the rest of the model was modelled with beam elements. The local fidelity of the model was tuned on-the-fly as required during the simulation, i.e, at any moment during the simulation, the *polymorphic* became more 'Continuum' as the crack tip approached them, and more '2-beam' as the crack tip became more distant.

For the 'Continuum' state, and as can be seen in Figure 13, 10 quadrilateral elements were assigned through the thickness (5 for each arm). The 'Continuum' state was meshed using 4-noded quadrilateral elements with linear shape functions. A plane-strain formulation was used with a full integration scheme. For the beam states, a 2-noded Euler-Bernoulli formulation was used. The initial values for the weight functions were such that the far end of the specimen in the direction of the wake of the crack tip was in the '2-beam' state, the part near the crack tip was in the 'Continuum' state, and the far end of the specimen ahead of the crack tip was in the '1-beam' state.

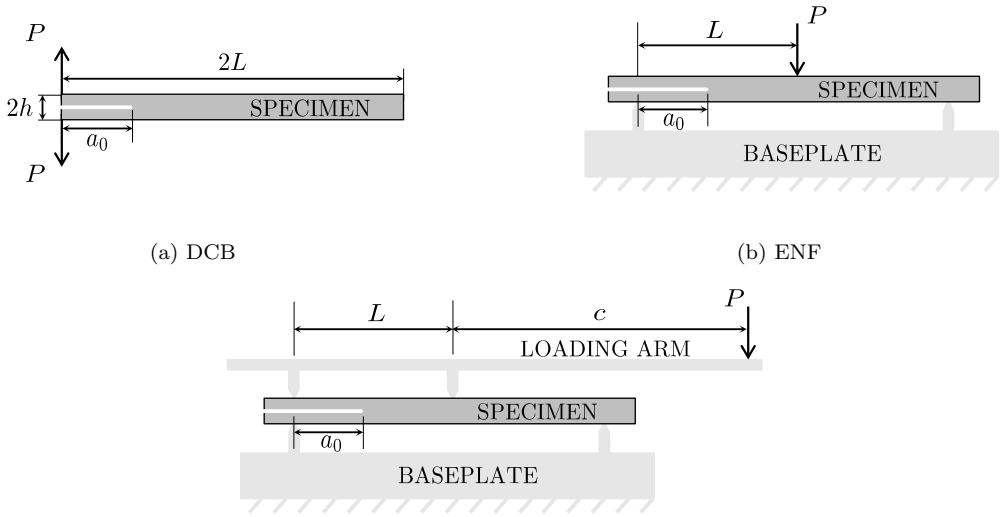

(a) DCB

(b) ENF

(c) MMB

Figure 11: Test specimens

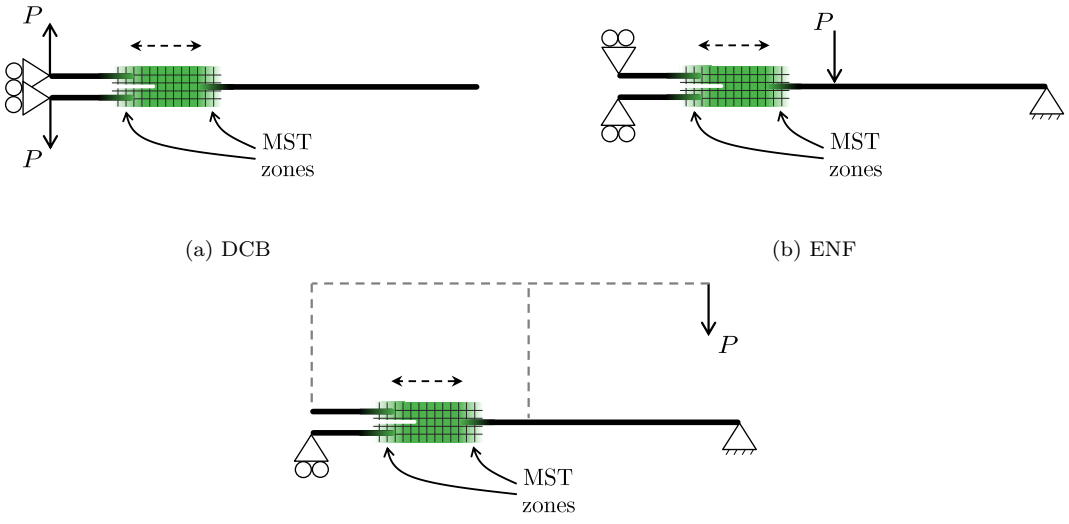

(a) DCB

(b) ENF

(c) MMB

Figure 12: Application of the *polymorphic* elements to the test cases

For the VCCT calculations, the methodology described in Section 7.3.1 was employed to simulate the delamination propagation. For the cohesive elements, a standard bi-linear law was used to simulate the regions in front of the crack tip (with properties given in Table 2, a quadratic stress interaction initiaton criterion, and the B-K propagation criterion).

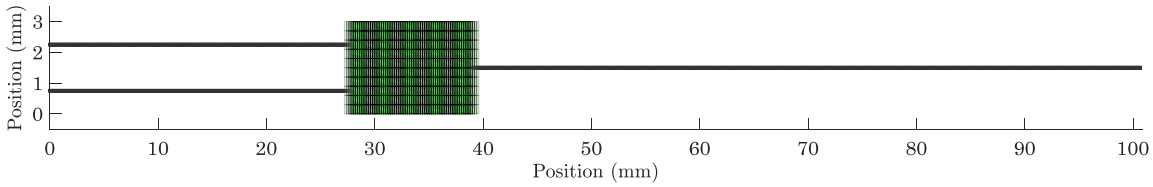

Figure 13: The mesh used for the test cases in its initial position

6.2. Double cantilever beam test

The schematic for the DCB test case is provided in Figures 11a and 12a. The test is designed to achieve mode I crack propagation throughout the loading.

In this simulation, the length of the continuum region in the wake and ahead of the crack tip were chosen to be 2 mm and 8 mm, respectively. The length of each individual element was 0.2 mm with an aspect ratio of 1.5, and the length of each MST zone was 0.8 mm.

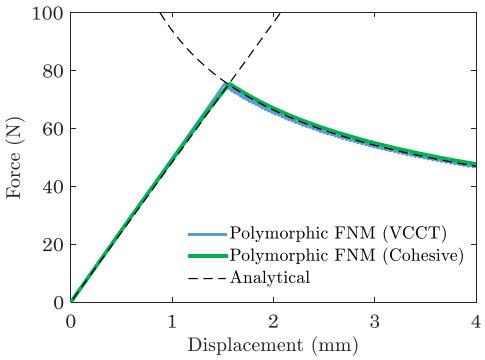

Figure 14: Force vs. opening displacement prediction

The force vs. opening displacement predictions are given in Figure 14. Results show good agreement between the *polymorphic* FNM predictions and the analytical solution using modified beam theory [56]. The evolution of the state of the polymorphic elements during the simulation can be seen in Figure 15. In Figure 15, the integration point positions of the cohesive elements are shown with empty circles. The line colour of the circles represents the damage of the cohesive element. The cohesive elements that have completely failed are shown with grey colour whereas the intact ones are shown with white colour.

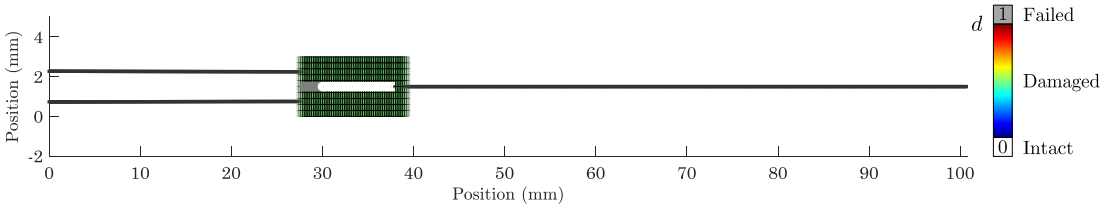

(a) State of the polymorphic elements at the start of the simulation

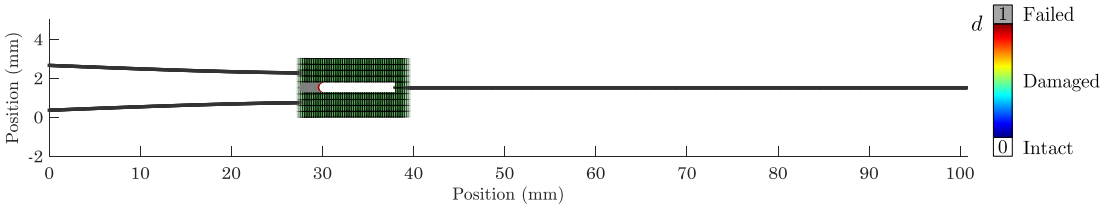

(b) State of the polymorphic elements at 1.6 mm applied displacement

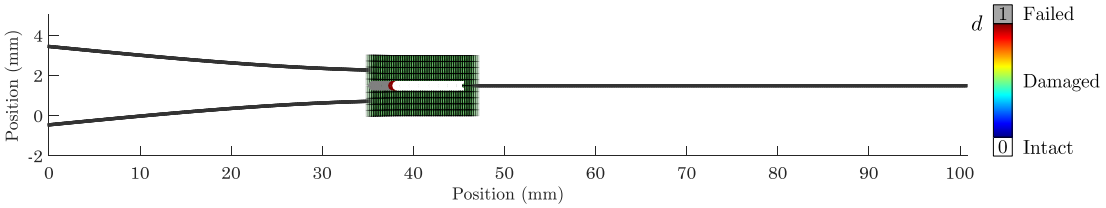

(c) State of the polymorphic elements at 2.4 mm applied displacement

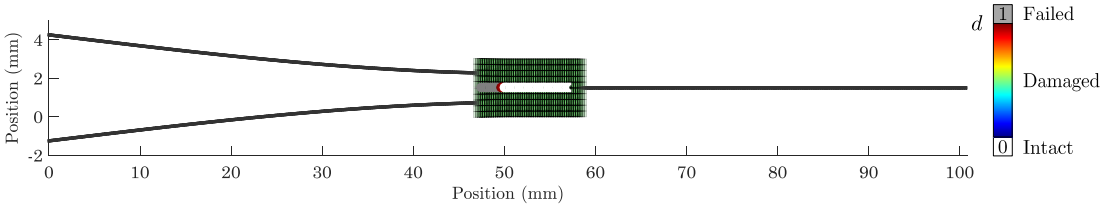

(d) State of the polymorphic elements at 4 mm applied displacement

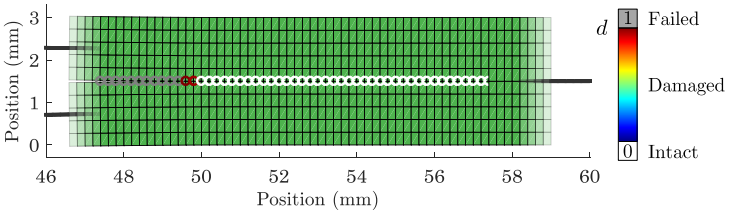

(e) Region near the crack tip at 4 mm applied displacement

Figure 15: Evolution of the state of the polymorphic elements for the DCB simulation

Using VCCT, a mesh convergence study was conducted using three different element lengths that are 0.2 mm, 0.3 mm, 0.4 mm in the horizontal direction. The results are shown in Figure 16.

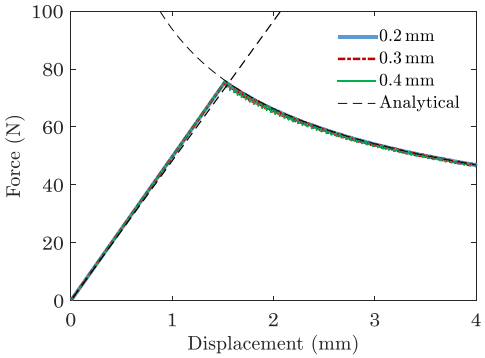

Figure 16: Mesh convergence study

Parametric studies were conducted for the length of the continuum region in the wake of and ahead of the crack tip and the length of the MST zone, also using VCCT. The results are given in Figure 17. The baseline values for the parameters were 3 mm, 12 mm for the length of the continuum region before and after the crack tip, and 1.2 mm for the length of the MST zone. The value of one parameter was changed keeping the others constant in each part of the parametric study.

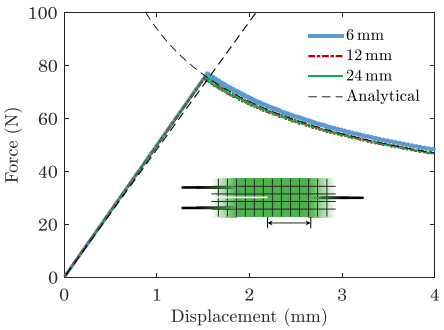

(a) Effect of the continuum zone length ahead of the crack tip

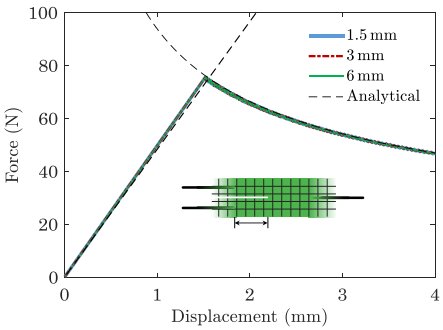

(b) Effect of the continuum zone length in the wake of the crack tip

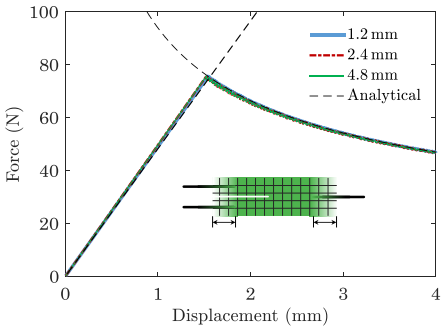

(c) Effect of the MST zone length

Figure 17: Parametric studies for the DCB test with VCCT

In Figure 17a, results during crack propagation for the model with a 6 mm continuum region ahead of the crack tip show load values higher than models with longer continuum regions. This is because the displacement field and the stress state around the crack tip are affected by the constraint equations linking the two states (see Appendix). Therefore, as the single-beam state approaches the crack tip, the energy release rate becomes less accurate. Finally, it can be inferred that a sufficiently large continuum region is needed for accurate representation of the crack. This is consistent with other results reported in the literature [14, 32]. Figures 17b and 17c show that the remaining baseline parameters are also converged.

6.3. End-notch flexure test

The schematic for the ENF test is provided in Figures 11b and 12b. The test is devised to obtain mode II crack propagation throughout the loading.

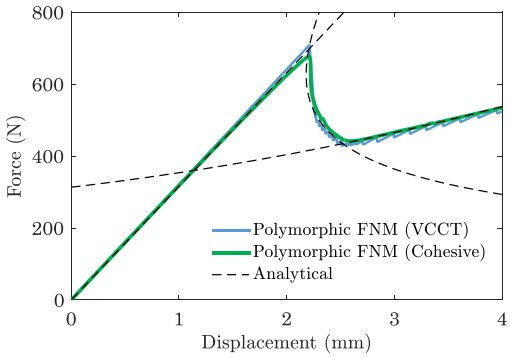

Figure 18: Force vs. opening displacement prediction

The simulations were conducted with the parameters and mesh lengths from the DCB test which were verified to provide converged results in this case. The force vs. opening displacement predictions are given in Figure 18. Results show good agreement between the *polymorphic* FNM predictions and the analytical solution. Moreover, the evolution of the state of the *polymorphic* elements during the simulation is also shown in Figure 19.

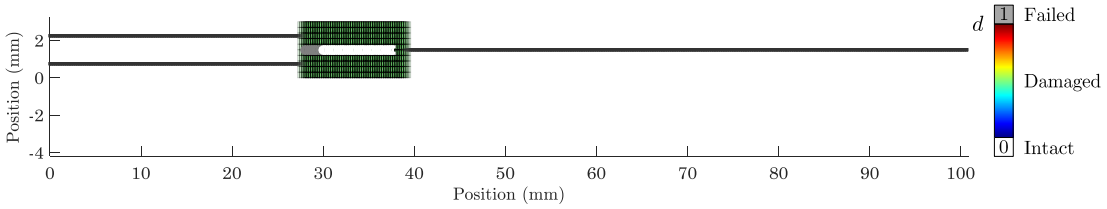

(a) State of the polymorphic elements at the start of the simulation

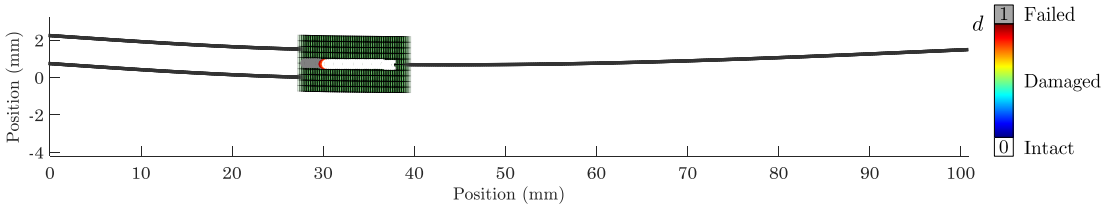

(b) State of the polymorphic elements at 1.6 mm applied displacement

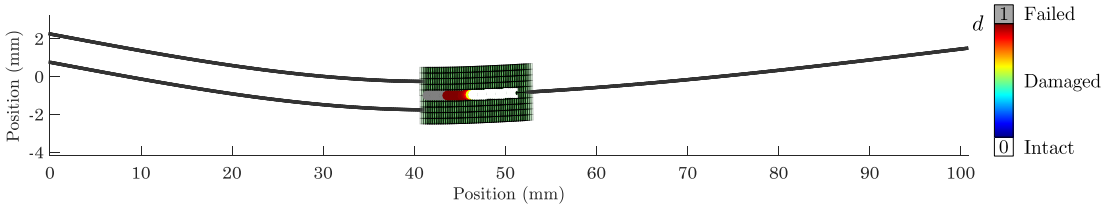

(c) State of the polymorphic elements at 2.4 mm applied displacement

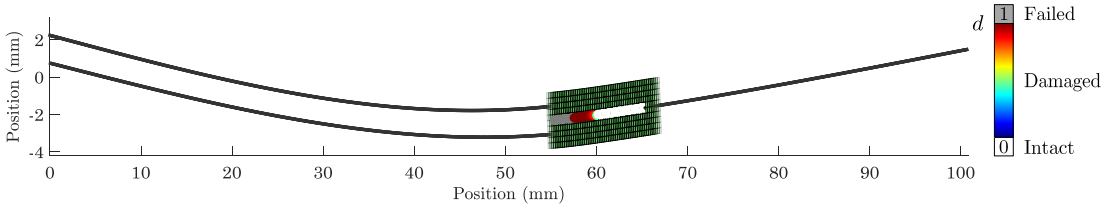

(d) State of the polymorphic elements at 4 mm applied displacement

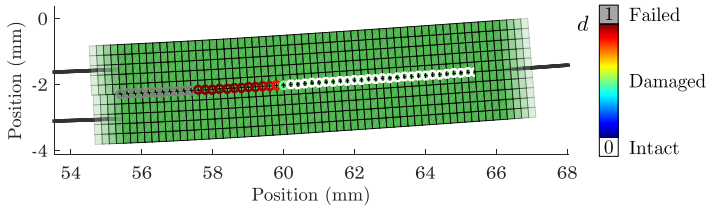

(e) Region near the crack tip at 4 mm applied displacement

Figure 19: Evolution of the state of the polymorphic elements for the ENF simulation

6.4. Mixed mode bending test

A schematic for the MMB test case is provided in Figures 11c and 12c. The test is devised to enforce mixed mode crack propagation with mode ratio of 0.5 throughout the loading. This is achieved by imposing $c = 41.3\,\text{mm}$.

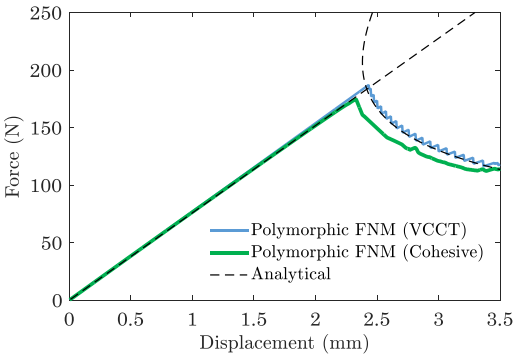

Figure 20: Force vs. opening displacement prediction

The simulations were conducted with the same converged parameters and mesh lengths. The loading arm was modelled with rigid elements. The force vs. opening displacement predictions are given in Figure 20. Results show excellent agreement between the polymorphic FNM predictions with VCCT and the analytical solution. For the *polymorphic* FNM model with cohesive elements, the agreement is acceptable, and the small error is related to the known difficulty with cohesive elements predicting correctly the mode ratio [57]. The evolution of the state of the polymorphic elements during the simulation can be seen in Figure 21.

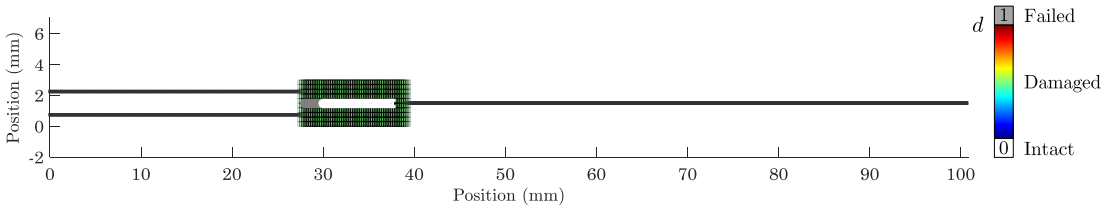

(a) State of the polymorphic elements at the start of the simulation

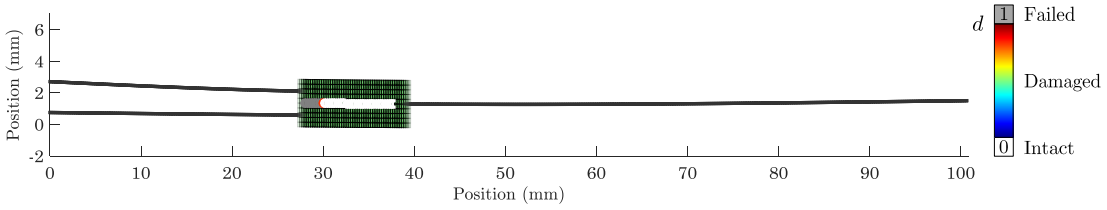

(b) State of the polymorphic elements at 1.6 mm applied displacement

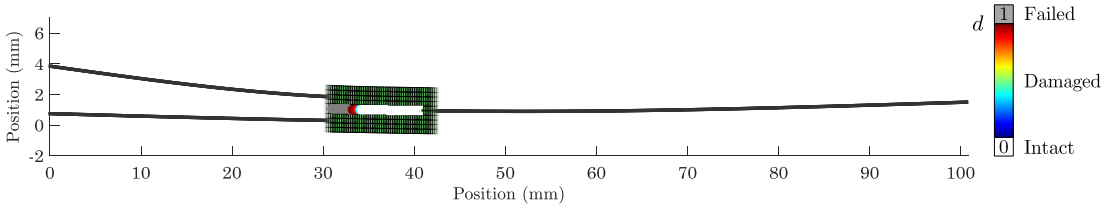

(c) State of the polymorphic elements at 2.4 mm applied displacement

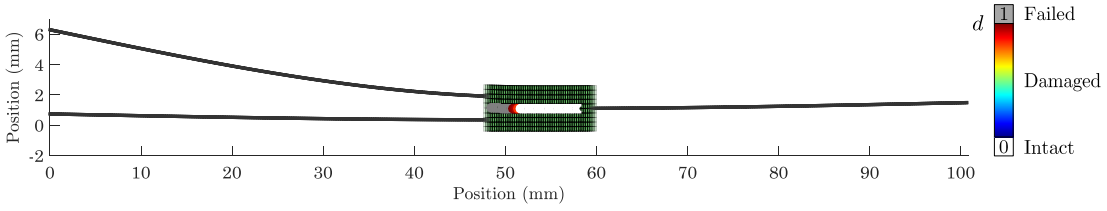

(d) State of the polymorphic elements at 4 mm applied displacement

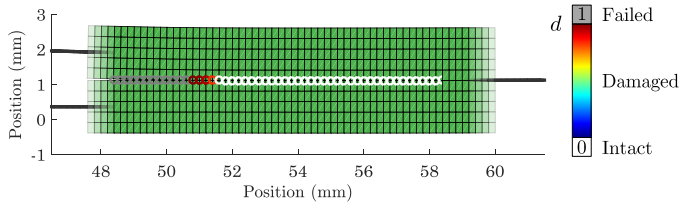

(e) Region near the crack tip at 4 mm applied displacement

Figure 21: Evolution of the state of the polymorphic elements for the MMB simulation

Figure 22 shows the CPU time reductions that were achieved when using the polymorphic elements models instead of fully-continuum models. Polymorphic element results (using either VCCT or cohesive zone model) are compared against fully-continuum models using the corresponding damage modelling technique (VCCT or cohesive zone model as appropriate). It can be concluded that the polymorphic element models

were computationally more efficient in all cases, with computational savings of about 70% when using cohesive elements, and of about 25% when using VCCT.

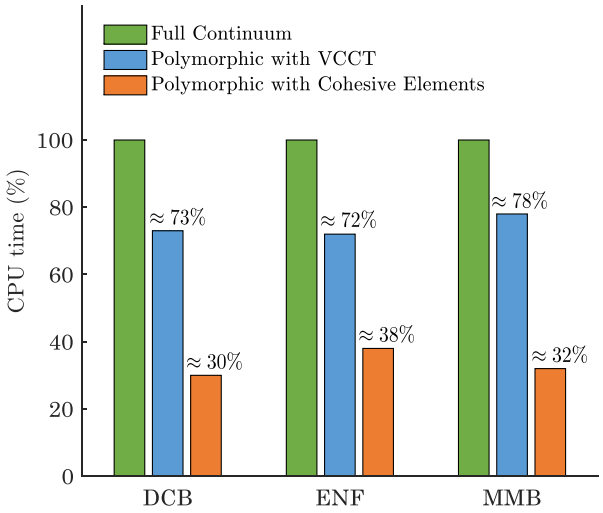

Figure 22: CPU time reduction for polymorphic element models, with VCCT and with Cohesive elements, with respect to the corresponding fully-continuum models

7. Application

7.1. Delamination migration test

In this section, the capability of the method for applications that involve a relatively complex damage mechanism is demonstrated. As an application case, a delamination-migration (DM) test that was proposed in the literature was selected [46]. De Carvalho et al. [47] demonstrated the applicability of FNM to simulate the DM test using continuum elements, and McElroy [14] demonstrated the same using a shell FNM formulation. In this section, the results obtained using the *polymorphic* FNM formulation were compared against the experimental and numerical results presented in the literature.

A schematic of the tests cases along with the geometrical properties are provided in Figure 23. The test involves loading a cross-ply laminate specimen, with an initial crack, that is clamped from the both ends. The specimen is composed of 44 plies and the stacking sequence is $[90_4/0_3/(90/0)_{2s}/0_2/0/90_4/\mathrm{T}/0/90_4/0_2/(90/0)_{2s}/0_2/90_3/0/90]$, where T refers to a PolyTetraFluoroEthylene (PTFE) insert defining the position of the initial crack along the thickness. The loading is applied to the top of the laminate with a distance L (load offset) apart from a clamped end. As the initial crack propagates, the crack that is initially at an interface between 0° and 90° plies migrates to an another 0°/90° interface to the top.

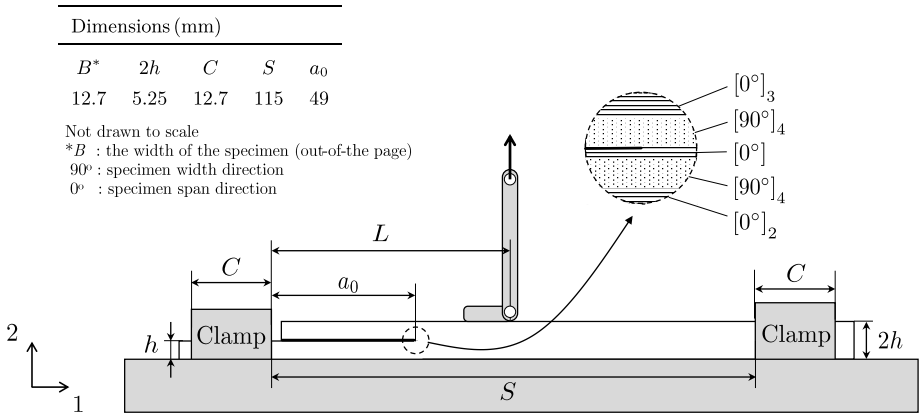

Figure 23: Delamination migration test schematic, after [47]

To demonstrate the proposed approach, four different displacement-controlled tests were simulated that involve application of different load offsets $L = a_0$, $1.1a_0$, $1.2a_0$, $1.3a_0$. VCCT was used to capture the crack propagation.

7.2. Numerical model

In order to model this test, a suitable realization of the *polymorphic* element was used as illustrated in Figures 24 and 25. In this realization, the *polymorphic* elements have three states. Two of these states are the '1-beam' (Figure 25d) and '2-beam' (Figure 25b) states also used in the previous section. The latter ('2-beam' state) can be used to represent the two arms both before and after the crack migration (by changing the bending stiffness and position of the neutral axes). The third state, which is used to simulate the region of the specimen near the crack tip, contains a suitable combination of continuum and beam elements (see Figure 25c) to model both delaminations and the migration with maximum numerical efficiency (and to demonstrate that the complexity of each state can be easily built up).

As shown inFigure 25c, this third state can in turn be partitioned in three different ways to simulate the required delaminations and ply cracking. The part of stacking sequence simulated with the continuum elements is $[0/90_4/\mathrm{T}/0]$. Each block of plies with the same orientation (through-thickness) was modelled with a separate element. The beams above and below the continuum region (see Figures 25a and 25c) were coupled with the continuum parts through suitable multi-point constraints.

As in the previous section, suitable multipoint constraints are used inside the polymorphic element formulation to enforce compatibility of displacements and rotations between its different states. For the continuum elements, first-order 4-noded quadrilateral elements were used with plane strain formulation and full integration scheme. For the beam elements, the respective plies were homogenized using classical lamination theory to obtain the equivalent elastic properties for the 2-noded Timoshenko beam elements.

In both cases, the material properties used are given in Tables 1 and 2. The mesh that was used for the simulations is shown in Figure 26. As the numerical system is different from the verification cases, a separate mesh convergence study was conducted to find the suitable length parameters for the wake and ahead of the crack tip in the higher fidelity state (Figure 25c).

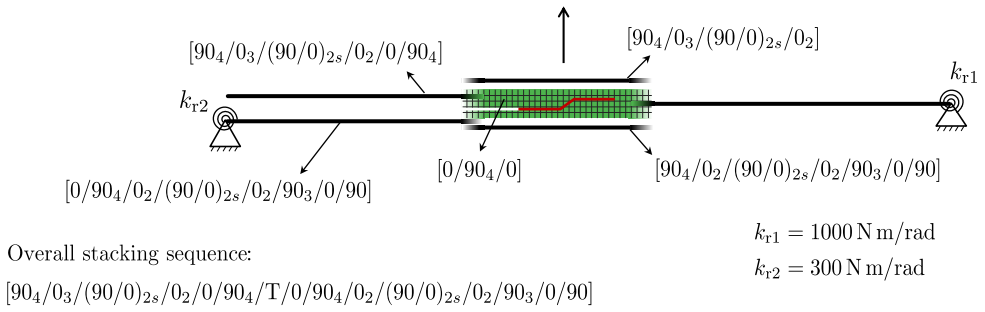

Figure 24: Application of the polymorphic elements to the DM test where the representative crack path is shown in red

The motivation for using a combined continuum/beam discretisation along the thickness was to achieve even better computational efficiency and to demonstrate the capability of the *polymorphic* elements to realize various discretizations on-the-fly. The constraint equations linking the beam and continuum parts at each relevant cross-section occur inside the *polymorphic* elements; hence, they do not need to be defined a priori in the FE model. The fact that this more efficient discretisation can be achieved in an automated way is an important feature of *polymorphic* elements.

In order to simulate the clamp parts of the specimen (see Figure 23), the beam ends of the numerical model (see Figure 24) were clamped both in the horizontal and vertical directions; additionally, to capture more realistically the effect of the clamps on bending, rotational springs were added to the beams at the clamped ends instead of fully fixing the rotation.

In this case, and unlike in the verification examples in section 6, we can choose to retain the use of continuum elements for representing the region where migration occurs (i.e. the coarsening of the region in the wake of crack tip can be de-activated when the migration occurs). In this case, the continuum region does not need to remain constant in size throughout the analysis. Alternatively, we can keep the continuum region constant in size, and, as the crack grows beyond the migration region, represent this region using a suitable '2-beam' state. Below, we will show results using both options.

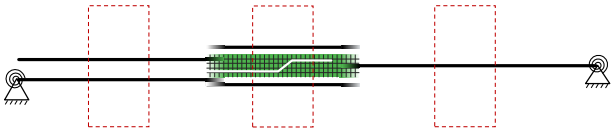

(a) Indication of different element states in the wake, vicinity and ahead of the crack tip

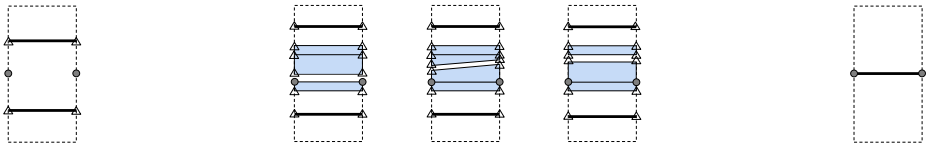

(b) State of the polymorphic element in the wake of the crack tip

(c) State of the polymorphic element in the vicinity of the crack tip, indicating three possible FNM partitions

(d) State of the polymorphic element ahead of the crack tip

Figure 25: Realisation of the polymorphic element for the DM test

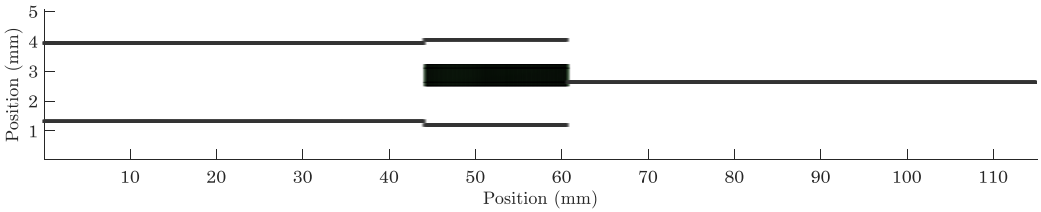

(a) Entire mesh for the DM specimen at the start of the simulation

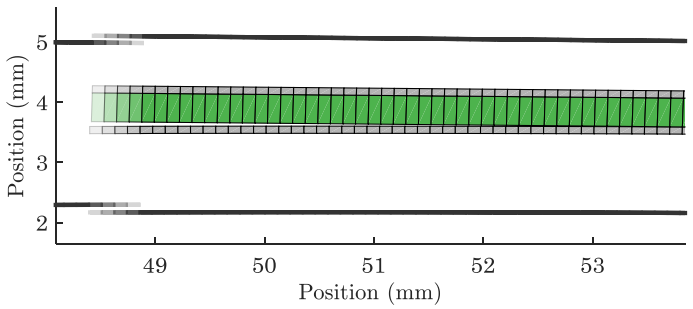

(b) Zoomed-in of the mesh near the crack tip during crack propagation

Figure 26: Mesh used for the DM simulation

7.3. Damage propagation criteria

7.3.1. Delamination

For delamination, we use the B-K criterion

$$\frac{G_{\mathrm{T}}}{G_{\mathrm{c}}} - 1 = 0, \tag{25}$$

where the total energy release rate G_{T} for delamination is

$$G_{\mathrm{T}} = G_{\mathrm{I}} + G_{\mathrm{II}}, \tag{26}$$

where G_{I} and G_{II} are the energy release rate in mode I and mode II, respectively, and the critical energy release rate for delamination is

$$G_{\mathrm{c}} = G_{\mathrm{Ic}} + (G_{\mathrm{IIc}} - G_{\mathrm{Ic}})(G_{\mathrm{II}}/G_{\mathrm{T}})^{\eta_{\mathrm{BK}}}, \tag{27}$$

where G_{Ic} and G_{IIc} are the critical energy release rates of the interface in mode I and II, and η_{BK} is the experimental interaction parameter.

7.3.2. Matrix cracking

As it is generally assumed for cracks propagating in isotropic materials, matrix cracks are assumed to follow a mode I fracture path perpendicular to the fibres [58]. Therefore, in the case of matrix cracking in composites, the total energy release rate is compared against the mode I intra-laminar critical energy release rate to determine the propagation. As is common in composites [59], the latter is approximated by the mode I critical energy release rate of the interface, G_{Ic}. Then, following [47] the overall criterion used for matrix cracking can be written as

$$\frac{G_{\mathrm{T}}}{G_{\mathrm{Ic}}} - 1 = 0 \quad \text{with} \quad G_{\mathrm{T}} = G_{\mathrm{I}} + G_{\mathrm{II}}. \tag{28}$$

7.3.3. Delamination migration

In composites, delamination migration occurs when delamination propagating at one interface kinks out of the interface by transitioning into a matrix crack and subsequently re-locates to another interface. The realization of the migration depends on several conditions that involve the stress state and fracture toughness of the interface. In the present study, an approach similar to the one described [47] was followed to determine the migration. Consider a crack between materials A and B (Figure 27), with a local coordinate system (t, n), subject to a shear loading. The internal tangential force at the node at the crack tip, defined as positive for a positive shear stress in the coordinate system (t, n), is F_{t}. Then the migration criterion based on [47] can be written as

$$\frac{G_{\mathrm{T}}}{G_{\mathrm{c}}} - 1 \geq 0 \quad \text{and} \quad \frac{G_{\mathrm{T}}}{G^{i}_{\mathrm{Ic}}(F_{\mathrm{t}})} - 1 \geq 0, \tag{29}$$

where $G^i_{\mathrm{Ic}}(F_{\mathrm{t}})$ refers to the mode I fracture toughness of the material to which the delamination kinks. $G^i_{\mathrm{Ic}}(F_{\mathrm{t}})$ is given by [47]

$$G^i_{\mathrm{Ic}}(F_{\mathrm{t}}) = \begin{cases} G^{\mathrm{A}}_{\mathrm{Ic}} & \Leftarrow \quad F_{\mathrm{t}} < 0 \\ G^{\mathrm{B}}_{\mathrm{Ic}} & \Leftarrow \quad F_{\mathrm{t}} > 0 \end{cases}. \tag{30}$$

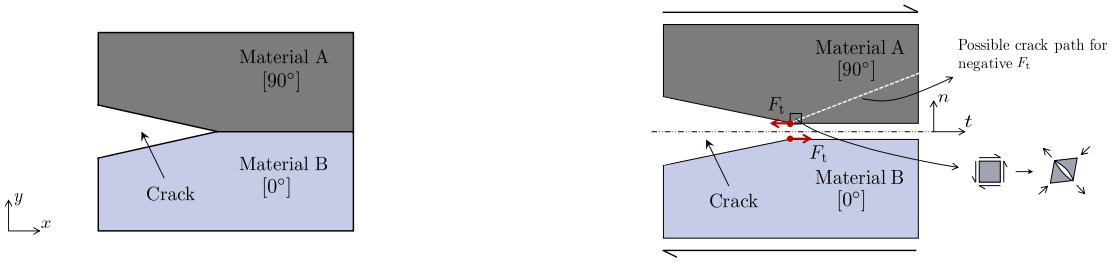

(a) Crack at a bimaterial interface

(b) The migration onset criterion

Figure 27: Migration of a crack at a bimaterial interface, after De Carvalho et al. [47]

The intralaminar fracture toughness of a 90° ply ($G^{\mathrm{A}}_{\mathrm{Ic}}$) can be approximated by the interlaminar toughness in Table 2. The translaminar toughness of a 0° ply ($G^{\mathrm{B}}_{\mathrm{Ic}}$) is orders of magnitude higher than $G^{\mathrm{A}}_{\mathrm{Ic}}$ in this example, and hence migration to the 0° ply does not occur. Therefore, the precise value used ($G^{\mathrm{B}}_{\mathrm{Ic}} = 91.6\mathrm{kJ/m}^2$ [60]) does not matter in practice.

Once delamination migration was predicted, the migration angle was calculated based on the maximum tangential stress criterion using the stresses at the crack tip node and calculating the corresponding principal stress angles.

7.4. Calibration of rotational springs

In order to find a suitable set of coefficients for the rotational springs, an experimental test case from De Carvalho et al. [47] was used for calibration. In this test case, the deflection of the specimen was captured experimentally via DIC (Figure 28) and used as a benchmark for calibration of the numerical deflections. In the test case, a prescribed displacement was applied to the top of the specimen with a distance $L = 0.98a_0$, and the initial crack length a_0 was 52.3 mm. Using this test case and the stiffness acquired from the load-displacement curve, the rotational spring coefficients $k_{\mathrm{r}1}$ and $k_{\mathrm{r}2}$ were calibrated to 1000 N m/rad and 300 N m/rad, respectively.

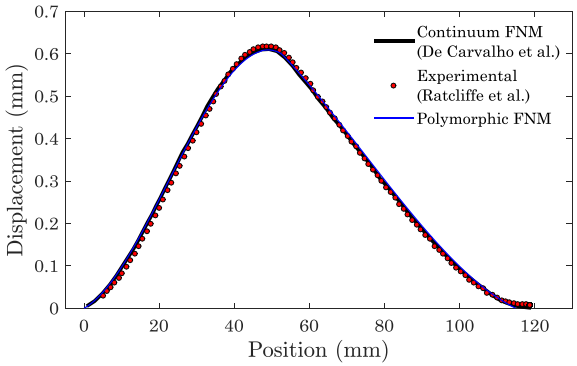

Figure 28: Deflection comparisons

7.5. Results

7.5.1. Predictions with constant vs. variable size of continuum region

The force vs. applied displacement curves for a load offset $L = 1.2a_0$ are shown in Figure 29, comparing the solutions in which we kept the size of the continuum region constant vs. the case in which we kept the migration region always represented with continuum elements. In this figure, it can be seen that both curves coincide. The evolution of the state of the *polymorphic* elements during the simulation for these two cases can be seen in Figure 30, and a zoom of the migration region is shown in Figure 31. In this case, the computational time for the model with constant size of the continuum region is 12% lower.

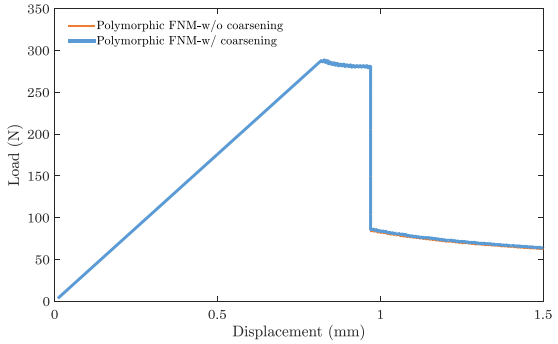

Figure 29: Force-displacement curves with and without coarsening in the wake of the crack

7.5.2. Comparison against literature

The force vs. applied displacement curves for different load offsets $L = a_0$, $1.1a_0$, $1.2a_0$, $1.3a_0$ are given in Figure 32 (in this section, we used the model with the migration region represented with continuum elements, but the results are the same for both models). In Figure 32, the current results correspond to the thick green line, together with continuum (black line, De Carvalho et al. [47]), shell (red line, McElroy

et al. [61]) and experimental (grey empty circles, Ratcliffe et al. [46]) results from the literature (the blue curve will be discussed later). The evolution of the state of the *polymorphic* elements during the simulation for the case $L = 1.2a_0$ can be seen in Figure 30.

In between points 2 and 4 (see Figure 32), upon detecting the instability, we only allow for damage to grow one element at the time with a constant applied displacement; the displacement is only allowed to grow again once damage has stopped growing. In this way, we were able to obtain several output points in between points 2 and 4 in Figure 32; this was crucial for identifying point 3.

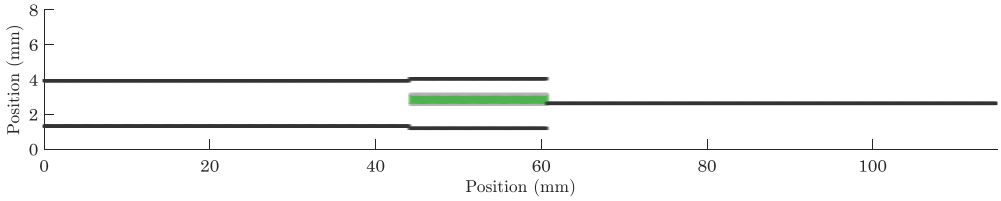

(a) Mesh at the start of the simulation

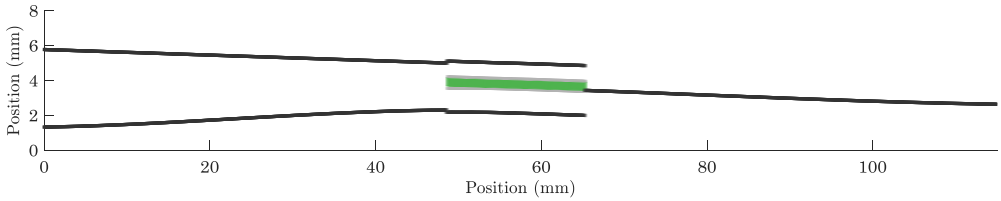

(b) Mesh at the stable crack propagation after the peak load

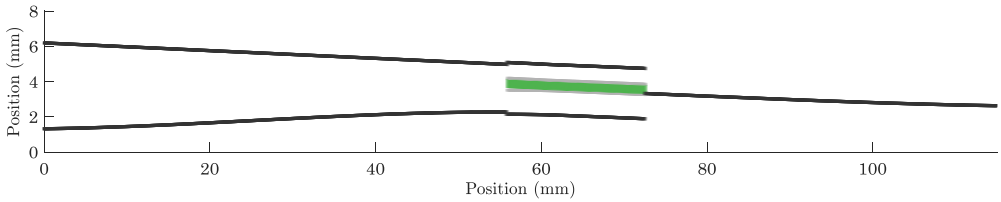

(c) Mesh during the sudden load drop just before migration

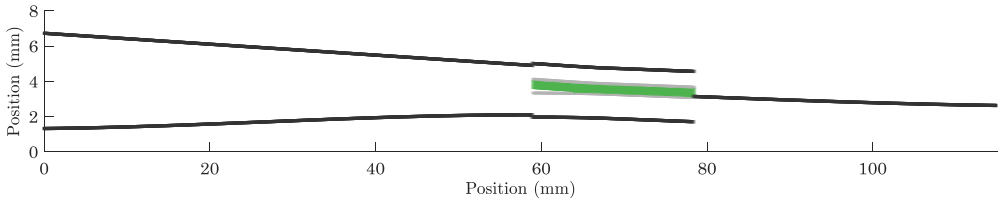

(d) Mesh during the sudden load drop just after migration

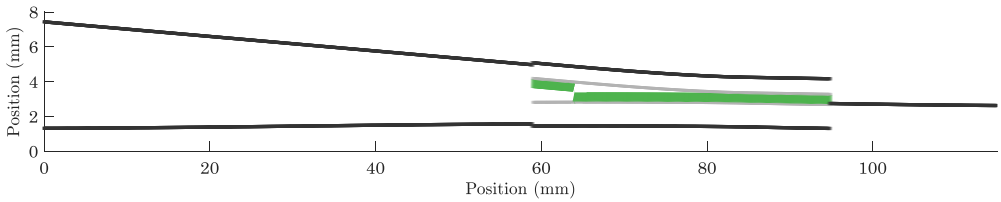

(e) Mesh during the last stable crack propagation stage

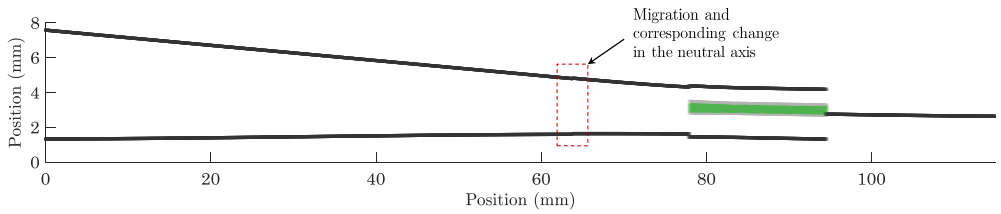

(f) Mesh during the last stable crack propagation stage when the higher fidelity zone is constant

Figure 30: Evolution of the overall mesh for the DM test for the case $L = 1.2a_0$

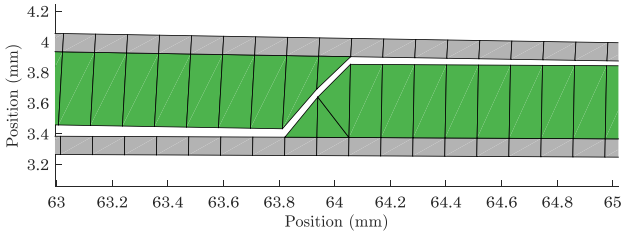

Figure 31: Zoom-in of the mesh during the sudden load drop just after migration

For the case $L = a_0$, when the system reaches the peak load, a sudden load drop is observed with unstable crack growth. Before crack migration, the unstable crack propagation stops and the load increases until 160 N before propagating to the next $[0°/90°]$ interface. Then, a second sudden load drop is observed with an unstable crack growth followed by the last stage where stable crack propagation occurs along the $[0°/90°]$ interface. A similar sequence of events was observed in the results from De Carvalho et al. [47].

For the rest of the load offsets $L = 1.1a_0$, $1.2a_0$, $1.3a_0$, stable crack propagation occurs after the peak load. The stable crack propagation is followed by the sudden load drop where the migration event happens. Finally, after the load drop, the system experiences a stable crack growth. Migration happens during the sudden load drop where unstable crack propagation is observed. Again, a similar sequence of events can be observed in the results from De Carvalho et al. [47] and McElroy et al. [61].

Simulations were also performed for all test cases but without permitting delamination migration, i.e. only delamination was permitted by the model (shown as the blue curves in Figure 32). As it can be observed in Figure 32, at the latter stages of the test, the *polymorphic* FNM results with migration compare favourably with the results from De Carvalho et al. [47], whereas preventing the possibility of migration leads to the results from McElroy et al. [61] at the final stable crack propagation stage.

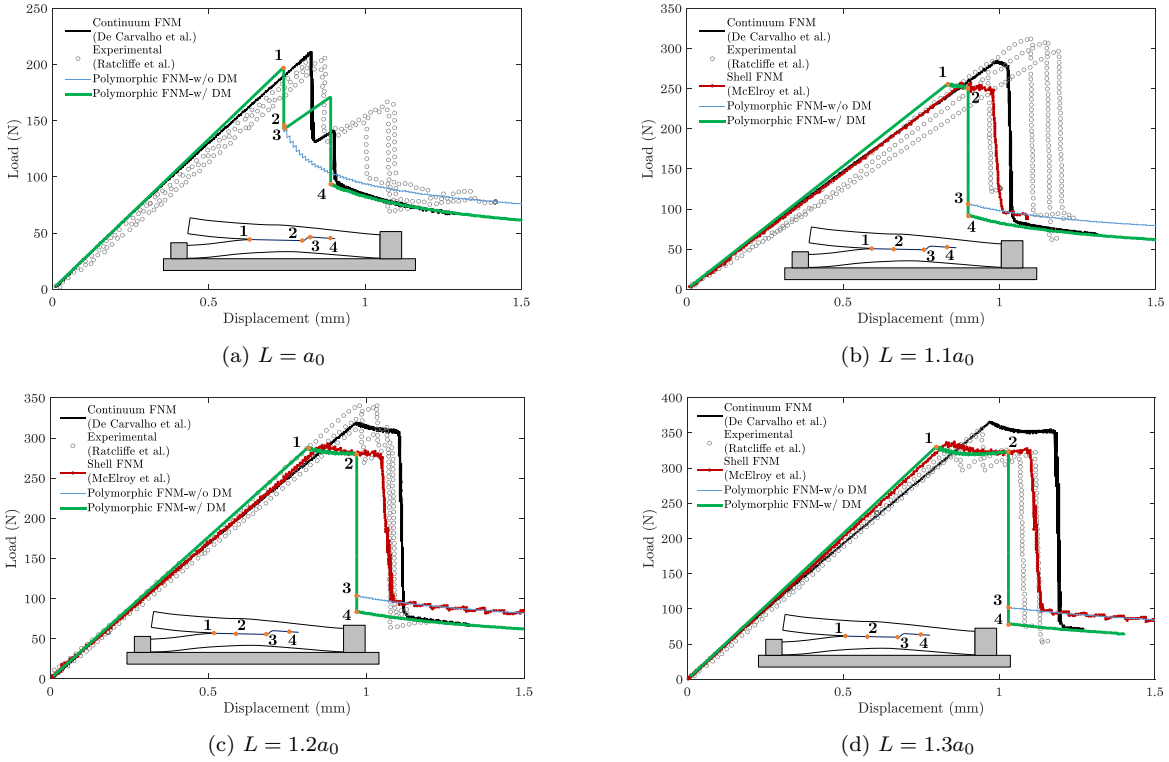

(a) $L = a_0$ (b) $L = 1.1a_0$

(c) $L = 1.2a_0$ (d) $L = 1.3a_0$

Figure 32: Force-displacement curves for different load offsets

In Table 3, the migration locations i.e. the distance between the initial crack tip and the start of the migration acquired from experimental and various numerical methods are provided together with the *polymorphic* FNM results.

Table 3: Distance between the delamination migration location and initial crack tip (mm)

	$L = a_0$	$L = 1.1a_0$	$L = 1.2a_0$	$L = 1.3a_0$
Continuum FNM [47]	58.1	62.4	66.0	69.8
Shell FNM [61]	-	70.0	73.0	77.0
Polymorphic FNM	55.9	59.9	63.8	67.7
Experimental [46]	57.5	66	67.5	71.5
Error	2.8%	9.2%	5.5%	5.3%

8. Discussion

Overall, the load-displacement results of the pure mode (Figures 14 and 18) and mixed mode (Figure 20) crack propagation tests show good agreement with the analytical results both for the VCCT and cohesive zone approaches for crack propagation.

The load-displacement response of the delamination migration tests (see Figure 32), as well as location of crack migration (Table 3), compare well with the experimental and numerical trends published in the literature. The peak loads predicted are generally in good agreement with the literature; this is especially true when comparing to predictions in the literature obtained using an enriched shell approach [61]. The latter is expected as most of the polymorphic model was composed of beam elements (making the polymorphic model relatively close to the enriched shell model).

Regarding the delamination migration case, the small differences between the different numerical results in the literature (see Figure 32) can be attributed to the difference in the element types used in the models and use of different numerical schemes to model the clamped parts of the delamination migration specimen. In the continuum model of De Carvalho et al. [47], the clamped parts were modelled explicitly, and the friction coefficients and clamping load were used for calibration to the experimental test case [47]. In the case of shell [14] and polymorphic element models, rotational springs have been introduced whose coefficients are used for calibration. Together with the dimensional differences, this motivates the small differences in the initial stiffnesses and also slight underestimation of the peak loads in the validation tests.

In accordance with the delamination migration criterion, delamination migration occurs when the shear sign of the tangential force changes. In the case where we have no migration, the change in shear sign triggers a stable crack propagation (blue curve). However, when we allow migration to occur, we observe further unstable crack growth along the new interface until point 4 (green curve).

The agreement between the application test results and the literature (see Figure 32 and Table 3) further demonstrates the applicability of the proposed polymorphic FNM for the simulation of tests involving complex damage mechanisms. The proposed polymorphic FNM has also potential to simulate complex damage mechanisms in three dimensional structures and the extension of the *polymorphic* element to 3D problems can be realized in-line with the methodology proposed in this work.

Moreover, the polymorphic FNM proves to be successful at extending the continuum region during the simulation as demonstrated in the delamination migration simulation (see Figure 30). Thus, the extent of the high-fidelity region can evolve efficiently and on-the-fly during a generic numerical simulation with the proposed methodology.

Using *polymorphic* FNM for multiscale analysis, we do not need to know a priori where damage will occur, which invalidates the use of most multiscale methods. Therefore, it makes sense to compare the computational efficiency of *polymorphic* FNM against competing single-scale models. With this in mind, the CPU time can be reduced by at least 70% (Figure 22) when compared to a single-scale simulation. However, the 70% CPU time reduction was obtained for a verification case where 6% of the mesh were continuum elements and 94% were structural elements. Clearly, as the proportion of structural elements in the mesh increases, the computational time saving should increase as well. Therefore, for a realistic, large, three-dimensional engineering structure, where only one single small location is to be modelled with

continuum elements but this location cannot be determined a priori, the *polymorphic* FNM can potentially provide even greater efficiency gains.

9. Conclusions

A new *polymorphic* Floating Node Method has been developed and implemented. This involves polymorphic elements which exhibit an evolving superposition of various states, each of which can have adaptive partitioning. For instance, a state may consist of a shell representation while another state may consist of a continuum representation. When applied in multiscale simulations, this new *polymorphic* FNM has as a key feature that the high-fidelity regions no longer need to be known a priori; instead, they are determined via an element-level management of the coupling between scales, and hence evolved during the analysis at element level. The following can be concluded:

- the *polymorphic* FNM can be integrated with VCCT and cohesive zone models to simulate damage propagation in pure and mixed-mode crack propagation scenarios;
- by using *polymorphic* FNM, each part of a structure can be modelled using the most suitable element type at each point during the simulation. Computational time saving of up to 70% was demonstrated in 2D examples involving crack propagation. Significantly, the computational efficiency depends on the simulated tests and can be potentially higher when modelling realistic-large scale engineering structures in 3D;
- the *polymorphic* FNM can be successfully applied to complex crack propagation scenarios as demonstrated by the modelling of a delamination migration test. The results demonstrate the potential impact of the proposed multiscale modelling approach for realistic engineering problems;
- overall, *polymorphic* FNM shows great potential for computationally-efficient multiscale modelling of large-scale structures and constitutes a new element technology whereby the fidelity of the elements can evolve during a numerical analysis and does not need to be defined a priori.

Acknowledgement

The first author greatly acknowledges the scholarship from The Scientific and Technological Research Council of Turkey (TUBITAK) and British Council in the framework of the programmes BIDEB-2213 and Newton-Katip Celebi Fund. The third author is grateful for the funding from EPSRC under grant EP/M002500/1.

Appendix: Constraint equations

Figure 33 provides an illustration to demonstrate the coupling between beam and continuum states. The constraint enforces compatibility between the degrees of freedom of the continuum elements along a cross section and those of the beam element as

$$u_i = u_\mathrm{b} + \theta z_i, \tag{31}$$

where u_b and u_i refer to the horizontal displacement DoF of the beam element at the neutral axis and of the continuum elements at node i, respectively (see Figure 33). θ is the rotational DoF of the beam element and z_i is the distance from the beam neutral axis for each node of the continuum state (see Figure 33). In addition, the vertical vertical displacement of the beam v_b is constrained to be equal to the vertical displacement of the the point in the continuum state at the neutral axis.

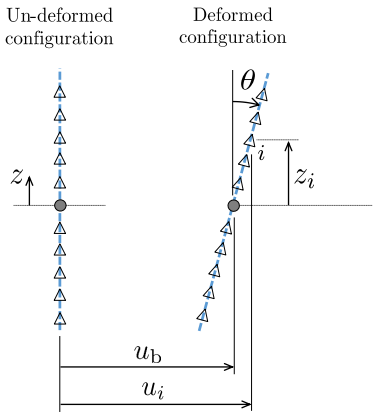

Figure 33: MPC implementation inside a *polymorphic* element

References

[1] V. M. F. Correia, M. A. A. Gomes, A. Suleman, C. M. M. Soares, C. A. M. Soares, Modelling and design of adaptive composite structures, Comput. Methods Appl. Mech. Eng. 185 (2-4) (2000) 325–346.

[2] U. Mandel, R. Taubert, R. Hinterhölzl, Laminate damage model for composite structures, Compos. Struct. 136 (2016) 441–449.

[3] R. Higuchi, T. Okabe, T. Nagashima, Numerical simulation of progressive damage and failure in composite laminates using XFEM/CZM coupled approach, Composites Part A 95 (2017) 197–207.

[4] F. Van der Meer, L. Sluys, A phantom node formulation with mixed mode cohesive law for splitting in laminates, Int. J. Fract. 158 (2) (2009) 107.

[5] F. Van Der Meer, L. Sluys, Continuum models for the analysis of progressive failure in composite laminates, J. Compos. Mater. 43 (20) (2009) 2131–2156.

[6] G. Alfano, M. Crisfield, Finite element interface models for the delamination analysis of laminated composites: mechanical and computational issues, Int. J. Numer. Methods Eng. 50 (7) (2001) 1701–1736.

[7] G. Alfano, F. M. de Sciarra, Mixed finite element formulations and related limitation principles: a general treatment, Comput. Methods Appl. Mech. Eng. 138 (1-4) (1996) 105–130.

[8] S. Heimbs, S. Heller, P. Middendorf, F. Hähnel, J. Weiße, Low velocity impact on CFRP plates with compressive preload: Test and modelling, Int. J. Impact Eng. 36 (10) (2009) 1182–1193.

[9] P. Areias, J. Song, T. Belytschko, Analysis of fracture in thin shells by overlapping paired elements, Comput. Methods Appl. Mech. Eng. 195 (41) (2006) 5343–5360.

[10] H. Qiao, W. Chen, Q. Yang, J. Lua, Augmented cohesive elements for efficient delamination analyses of composite laminates, J. Eng. Mater. Technol. 133 (4) (2011) 041010.

[11] C. Dávila, P. Camanho, A. Turon, Effective simulation of delamination in aeronautical structures using shells and cohesive elements, Journal of Aircraft 45 (2) (2008) 663–672.

[12] J. Reinoso, A. Blázquez, Application and finite element implementation of 7-parameter shell element for geometrically nonlinear analysis of layered CFRP composites, Compos. Struct. 139 (2016) 263–276.

[13] S. Zheng, C. Sun, A double-plate finite-element model for the impact-induced delamination problem, Compos. Sci. Technol. 53 (1) (1995) 111–118.

[14] M. McElroy, An enriched shell finite element for progressive damage simulation in composite laminates, Langley Research Center NASA/TP-2016-219211.

[15] R. Larsson, A discontinuous shell-interface element for delamination analysis of laminated composite structures, Comput. Methods Appl. Mech. Eng. 193 (30) (2004) 3173–3194.

[16] A. Ahmed, F. Van der Meer, L. Sluys, A geometrically nonlinear discontinuous solid-like shell element (DSLS) for thin shell structures, Comput. Methods Appl. Mech. Eng. 201 (2012) 191–207.

[17] J. Brouzoulis, M. Fagerström, Modelling of multiple delaminations in shells using XFEM, in: Proceedings for the 19th international conference on composite materials (ICCM19), 2013.

[18] J. Brouzoulis, M. Fagerström, An enriched shell element formulation for efficient modeling of multiple delamination propagation in laminates, Compos. Struct. 126 (2015) 196–206.

[19] M. McElroy, R. Gutkin, M. Pankow, Interaction of delaminations and matrix cracks in a CFRP plate, Part II: Simulation using an enriched shell finite element model, Composites Part A 103 (2017) 252–262.

[20] J. Reinoso, A. Blázquez, A. Estefani, F. París, J. Cañas, E. Arévalo, F. Cruz, Experimental and three-dimensional global-local finite element analysis of a composite component including degradation process at the interfaces, Composites Part B 43 (4) (2012) 1929–1942.

[21] J. Reinoso, A. Blázquez, A. Estefani, F. París, J. Canas, A composite runout specimen subjected to tension–compression loading conditions: Experimental and global–local finite element analysis, Compos. Struct. 101 (2013) 274–289.

[22] Y. Sato, T. Okabe, R. Higuchi, K. Yoshioka, Multiscale approach to predict crack initiation in unidirectional off-axis laminates, Adv. Compos. Mater 23 (5-6) (2014) 461–475.

[23] M. Akterskaia, E. Jansen, S. Hühne, R. Rolfes, Efficient progressive failure analysis of multi-stringer stiffened composite panels through a two-way loose coupling global-local approach, Compos. Struct. 183 (2018) 137–145.

[24] M. Paggi, M. Corrado, I. Berardone, A global/local approach for the prediction of the electric response of cracked solar cells in photovoltaic modules under the action of mechanical loads, Eng. Fract. Mech. 168 (2016) 40–57.

[25] S. Hühne, J. Reinoso, E. Jansen, R. Rolfes, A two-way loose coupling procedure for investigating the buckling and damage behaviour of stiffened composite panels, Compos. Struct. 136 (2016) 513–525.

[26] M. G. Geers, V. G. Kouznetsova, K. Matouš, J. Yvonnet, Homogenization Methods and Multiscale Modeling: Nonlinear Problems, Encyclopedia of Computational Mechanics Second Edition (2017) 1–34.

[27] J. Fish, Bridging the scales in nano engineering and science, J. Nanopart. Res. 8 (5) (2006) 577–594.

[28] J. Fish, Multiscale methods: bridging the scales in science and engineering, Oxford University Press on Demand, 2010.

[29] P. Kanouté, D. Boso, J. Chaboche, B. Schrefler, Multiscale methods for composites: a review, Arch. Comput. Methods Eng. 16 (1) (2009) 31–75.

[30] R. McCune, C. Armstrong, D. Robinson, Mixed-dimensional coupling in finite element models, Int. J. Numer. Methods Eng. 49 (6) (2000) 725–750.

[31] R. Krueger, J. Ratcliffe, P. Minguet, Panel stiffener debonding analysis using a shell/3D modeling technique, Compos. Sci. Technol. 69 (14) (2009) 2352–2362.

[32] R. Krueger, T. O'Brien, A shell/3D modeling technique for the analysis of delaminated composite laminates, Composites Part A 32 (1) (2001) 25–44.

[33] H. B. Dhia, G. Rateau, The Arlequin method as a flexible engineering design tool, Int. J. Numer. Methods Eng. 62 (11) (2005) 1442–1462.

[34] L. Gigliotti, S. Pinho, Multiple length/time-scale simulation of localized damage in composite structures using a Mesh Superposition Technique, Compos. Struct. 121 (2015) 395–405.

[35] P. R. Budarapu, R. Gracie, S. P. Bordas, T. Rabczuk, An adaptive multiscale method for quasi-static crack growth, Comput. Mech. 53 (6) (2014) 1129–1148.

[36] H. Talebi, M. Silani, S. P. Bordas, P. Kerfriden, T. Rabczuk, A computational library for multiscale modeling of material failure, Comput. Mech. 53 (5) (2014) 1047–1071.

[37] H. Talebi, M. Silani, T. Rabczuk, Concurrent multiscale modeling of three dimensional crack and dislocation propagation, Adv. Eng. Software 80 (2015) 82–92.

[38] P. R. Budarapu, J. Reinoso, M. Paggi, Concurrently coupled solid shell-based adaptive multiscale method for fracture, Comput. Methods Appl. Mech. Eng. 319 (2017) 338–365.

[39] S. Xiao, T. Belytschko, A bridging domain method for coupling continua with molecular dynamics, Comput. Methods Appl. Mech. Eng. 193 (17-20) (2004) 1645–1669.

[40] T. Belytschko, S. Xiao, Coupling methods for continuum model with molecular model, Int. J. Multiscale Comput. Eng. 1 (1).

[41] A. A. Wilmes, S. T. Pinho, A coupled mechanical-charge/dipole molecular dynamics finite element method, with multi-scale applications to the design of graphene nano-devices, Int. J. Numer. Methods Eng. 100 (4) (2014) 243–276.

[42] Y. Lee, C. Basaran, A multiscale modeling technique for bridging molecular dynamics with finite element method, J. Comput. Phys. 253 (2013) 64–85.

[43] J. Rojek, E. Oñate, Multiscale analysis using a coupled discrete/finite element model, Interaction and Multiscale Mechanics 1 (1) (2007) 1–31.

[44] B. Chen, S. Pinho, N. De Carvalho, P. Baiz, T. Tay, A floating node method for the modelling of discontinuities in composites, Eng. Fract. Mech. 127 (2014) 104–134.

[45] B. Chen, T. Tay, S. Pinho, V. Tan, Modelling the tensile failure of composites with the floating node method, Comput. Methods Appl. Mech. Eng. 308 (2016) 414–442.

[46] J. Ratcliffe, M. Czabaj, T. O'Brien, A test for characterizing delamination migration in carbon/epoxy tape laminates, NASA/TM–2013-218028, NASA, 2013 .

[47] N. De Carvalho, B. Chen, S. Pinho, J. Ratcliffe, P. Baiz, T. Tay, Modeling delamination migration in cross-ply tape laminates, Composites Part A 71 (2015) 192–203.

[48] B. Chen, T. Tay, S. Pinho, V. Tan, Modelling delamination migration in angle-ply laminates, Compos. Sci. Technol. 142 (2017) 145–155.

[49] X. Lu, B. Chen, V. Tan, T. Tay, Adaptive floating node method for modelling cohesive fracture of composite materials,

Eng. Fract. Mech. 194 (2018) 240–261.

[50] X. Lu, B. Chen, V. Tan, T. Tay, A separable cohesive element for modelling coupled failure in laminated composite materials, Composites Part A 107 (2018) 387–398.

[51] R. Krueger, Virtual crack closure technique: history, approach, and applications, Appl. Mech. Rev. 57 (2) (2004) 109–143.

[52] M. Ortiz, A. Pandolfi, Caltech ASCI technical report 090, Int. J. Numer. Methods Eng. 44.

[53] S. Osher, J. Sethian, Fronts propagating with curvature-dependent speed: algorithms based on Hamilton-Jacobi formulations, J. Comput. Phys. 79 (1) (1988) 12–49.

[54] L. Gigliotti, Multiscale analysis of damage-tolerant composite sandwich structures, Ph.D. thesis, Imperial College London, (2016) .

[55] R. Krueger, Development and application of benchmark examples for mixed-mode I/II quasi-static delamination propagation predictions, NASA/CR-2012-217562, NASA, 2012 .

[56] J. Williams, The fracture mechanics of delamination tests, J. Strain Anal. Eng. Des. 24 (4) (1989) 207–214.

[57] A. Turon, P. Camanho, J. Costa, J. Renart, Accurate simulation of delamination growth under mixed-mode loading using cohesive elements: definition of interlaminar strengths and elastic stiffness, Compos. Struct. 92 (8) (2010) 1857–1864.

[58] J. Hutchinson, Z. Suo, Mixed mode cracking in layered materials, in: Advances in applied mechanics, vol. 29, Elsevier, 63–191, 1991.

[59] S. Pinho, P. Robinson, L. Iannucci, Developing a four point bend specimen to measure the mode I intralaminar fracture toughness of unidirectional laminated composites, Compos. Sci. Technol. 69 (7) (2009) 1303–1309.

[60] S. T. Pinho, P. Robinson, L. Iannucci, Fracture toughness of the tensile and compressive fibre failure modes in laminated composites, Composites science and technology 66 (13) (2006) 2069–2079.

[61] M. McElroy, Use of an enriched shell finite element to simulate delamination-migration in a composite laminate, Compos. Struct. 167 (2017) 88–95.